NON-DESTRUCTIVE TESTING OF MATERIALS WITH THE DIFFERENTIAL GAMMA SCATTERING SPECTROSCOPY (DGSS) TECHNIQUE

BY

LARRY L. HUMPHRIES

A DISSERTATION PRESENTED TO THE GRADUATE SCHOOL
OF THE UNIVERSITY OF FLORIDA IN
PARTIAL FULFILLMENT OF THE REQUIREMENTS
FOR THE DEGREE OF DOCTOR OF PHILOSOPHY

UNIVERSITY OF FLORIDA

1989

Copyright 1989

By

Larry L. Humphries

ACKNOWLEDGEMENT

I gratefully acknowledge Dr. Samim Anghaie for his patience, enthusiasm and willing guidance.

This work was supported by the National Science Foundation under a grant for Small Business Innovative Research (SBIR).

TABLE OF CONTENTS

Page

ACKNOWLEDGEMENT iii
LIST OF TABLES vi
LIST OF FIGURES vii
ABSTRACT xiii

CHAPTERS

1 INTRODUCTION 1

2 NON-DESTRUCTIVE EXAMINATION BACKGROUND 6

Ultrasonic Testing 7
Radiation Scattering Methods 13
Infrared Thermography 25
Eddy Current Testing 28

3 DIFFERENTIAL GAMMA SCATTERING SPECTROSCOPY METHODS 32

Multiple Interactions 39
The Direct Spectrum 42
Development of Transport Equations 47

4 INVERSE TRANSPORT METHODS 64

Simple Matrix Inversion 64
Method of Least Square Fit 68

5 DATA CORRECTION METHODS 79

Compton Energy Broadening 79
Statistics 82

6 EXPERIMENTATION AND RESULTS 94

Gamma-ray Source 94
Test Samples 96
Detector 100
Detector Response 107
Detector Position 113

7 RESULTS AND DISCUSSION 127

Detection of Flaw 127

Page
Determination of Flaw Location 131
Determination of Flaw Size 136

8 CONCLUSIONS 148

APPENDICES

A MONTE CARLO CALCULATIONS 157

B DIFFERENTIAL SPECTRA 172

REFERENCES 203

BIOGRAPHICAL SKETCH 206

LIST OF TABLES

1 Probability, P_n, that n channels of the DGS display statistically significant deviations for a reference sample collected in 64,000 sec. 93

2 Comparison of integral of differential spectrum to the volume of the beam/flaw intersection 136

LIST OF FIGURES

Page

1 Ideal ultrasonic wave oscillations 9

2 Photon-electron scattering interaction 16

3 Polar plot of the Klein-Nishina formula for the Compton cross-section 18

4 Compton scattering NDE techniques 19

5 Computerized axial tomography 21

6 Computerized axial tomography scan 23

7 Eddy current probe 29

8 Variation of scattering angle with position of flaw along illuminated chord 34

9 Definition of differential spectrum 36

10 Ideal single scattered differential spectrum for a 0.25 cm hole located along the illuminated chord at three distances from point of beam entry 38

11 Multiple scattering events contributing to the differential spectrum 41

12 Direct scattering for a 2.5 cm sample 43

13 Multiple scattering factor for a differential spectrum from a 2.5 cm test piece with a 0.25 cm central hole 45

14 Multiple scattering factor for a direct spectrum from a 2.5 cm test piece with a 0.25 cm central hole 46

15 Ratio of calculated differential spectrum to direct spectrum for a 2.5 cm test piece with a 0.25 cm central hole 48

16 Geometry for twice scattered spectrum 56

Page

17 Comparison of Monte Carlo and discrete elements calculation of single scattered spectrum for a centrally located 0.25 cm hole. 58

18 Monte Carlo calculation of once and twice scattered spectrum incident on detector 59

19 Discrete elements calculation of once and twice scattered spectra incident on the detector 60

20 Monte Carlo calculation of differential spectrum from a 0.25 cm hole located at $x = 0.626$, $z=1.25$ cm 62

21 Monte Carlo calculation for a 0.25 cm hole located at $x=-.625$, $z=1.25$ cm. 63

22 Pixel representation of illuminated chord used for calculation of the differential spectrum 66

23 Selection of scattering energies to guarantee an upper triangular scattering matrix 69

24 Calculation of density profile along illuminated chord by least square method using exactly calculated differential spectra 75

25 Calculation of density profile along illuminated chord by least square method using measured differential spectra 77

26 Differential cross-section showing compton broadening at a scattering angle of 90^0 81

27 Calculated Compton broadening FWHM for a photon with energy 59.4 keV scattering in aluminum 83

28 Calculated Compton broadening FWHM for a photon with energy 661.6 keV scattering in aluminum 84

29 Calculated Compton broadening FWHM for a photon with energy 661.6 keV scattering in iron 85

30 Time elapsed view of differential spectrum 88

31 Test specimen for sensitivity study of hole location 98

32 Test specimen for detection of three holes 95

Page

33 Test specimen for outer wall thinning 101

34 Test specimen for inner wall thinning 102

35 Test specimen for pipe with four implanted service flaws 103

36 Calculated detector response to total scattered radiation field from central hole 110

37 Calculated detector response to singly scattered radiation field from eight hole locations 112

38 Single scattered differential spectrum from three detector locations in a 2.5 cm test specimen for a 0.25 cm central hole and a 4.53 cm detector . . 114

39 Projection of a point onto the illuminated chord . 115

40 Fractional resolution function 117

41 Ideal single scattered differential spectra for a 0.25 cm hole located along the illuminated chord at three distances from the beam point of entry. . . 118

42 Ideal single scattered differential spectra for a 0.25 cm hole located along the illuminated chord at three distances from point of entry 119

43 Monte Carlo calculated once and twice scattered spectra for a 0.25 cm central hole 121

44 Multiple scattering factor for a 0.25 cm central hole 122

45 Multiple scattering factor for a 0.25 cm central hole 123

46 Multiple scattering factor for a 0.25 cm central hole 124

47 Comparison of DGS for two detector positions . . . 126

48 The differential spectrum for three flaws together with the spectra from one central hole 130

49 Differential spectra for three flaw locations along the illuminated chord 132

Page

50 Differential spectra for two flaws not on the illuminated chord 133

51 Variation in differential spectra with pit location in pipe sample 135

52 Differential spectrum for 0.75 cm centrally located hole 137

53 Differential spectrum for 0.50 cm centrally located hole 138

54 Differential spectrum for 0.25 cm centrally located hole 139

55 Differential spectrum for 0.25 cm centrally located hole 140

56 Differential spectra for 0.635 cm diameter pit on inside wall of pipe 142

57 Differential spectra for 1.27 cm diameter pit on inside wall of pipe 143

58 Differential spectra for 0.635 cm wide gouge on inside wall of pipe 144

59 The difference between the DGS for a 1.27 cm diameter pit, and a 0.635 cm diameter pit 145

60 Diagram of pipe, pit, and detector geometry showing those scattered gamma-rays contributing to the differential spectra 146

61 Diagram of position sensitive detector 155

A.1 Calculation of new direction cosines from current direction cosines and scattering angles 161

A.2 Flow chart for Monte Carlo calculation of the differential spectrum from a hole located on the illuminated chord 166

A.3 Flow chart for the Monte Carlo calculation of the differential spectrum from a hole not located on the illuminated chord 168

A.4 Flow chart for the Monte Carlo calculation of the differential spectrum from a hole not located on the illuminated chord 169

Page

B.1 DGS for a 0.75 cm flaw located at x=0, z=0.625 cm in a 2.5 cm aluminum cylinder 173

B.2 DGS for a 0.75 cm flaw located at x=0, z=1.625 cm in a 2.5 cm aluminum cylinder 174

B.3 DGS for a 0.75 cm flaw located at x=0, z=1.875 cm in a 2.5 cm aluminum cylinder 175

B.4 DGS for a 0.75 cm flaw located at x=-.625, z=1.25 cm in a 2.5 cm aluminum cylinder 176

B.5 DGS for a 0.75 cm flaw located at x=.625, z=1.25 cm in a 2.5 cm aluminum cylinder 177

B.6 DGS for a 0.50 cm flaw located at x=0, z=0.625 cm in a 2.5 cm aluminum cylinder 178

B.7 DGS for a 0.50 cm flaw located at x=0, z=1.25 cm in a 2.5 cm aluminum cylinder 179

B.8 DGS for a 0.50 cm flaw located at x=0, z=1.875 cm in a 2.5 cm aluminum cylinder 180

B.9 DGS for a 0.50 cm flaw located at x=-.625, z=1.25 cm in a 2.5 cm aluminum cylinder 181

B.10 DGS for a 0.50 cm flaw located at x=0.625, z=0.625 cm in a 2.5 cm aluminum cylinder 182

B.11 DGS for a 0.25 cm flaw located at x=0, z= 0.625 cm in a 2.5 cm aluminum cylinder 183

B.12 DGS for a 0.25 cm flaw located at x=0, z= 1.25 cm in a 2.5 cm aluminum cylinder 184

B.13 DGS for a 0.25 cm flaw located at x=0, z= 1.875 cm in a 2.5 cm aluminum cylinder 185

B.14 DGS for a 0.25 cm flaw located at x=0.625,k z= 1.25 cm in a 2.5 cm aluminum cylinder 186

B.15 DGS for a 0.25 cm flaw located at x=.625, z=1.25 cm in a 2.5 cm aluminum cylinder 187

B.16 DGS for a 0.10 cm flaw located at x=0, z= 0.625 cm in a 2.5 cm aluminum cylinder 188

B.17 DGS for a 0.10 cm flaw located at x=0, z=1.25 cm in a 2.5 cm aluminum cylinder 189

Page

B.18 DGS for a 0.10 cm flaw located at x=0, z=1.875 cm in a 2.5 cm aluminum cylinder 190

B.19 DGS for a 0.10 cm flaw located at x=.625, z= 1.25 cm in a 2.5 cm aluminum cylinder 191

B.20 DGS for three flaws located along the illuminated chord 192

B.21 DGS for a 0.635 cm thick, 3.81 cm pipe with 0.3175 cm thinning on outside wall 193

B.22 DGS from a 5.08 cm O.D. pipe with a nominal 2.54 cm inner diameter showing internal wall thinning . . 194

B.23 DGS for a 0.635 cm diameter pit in a .3175 cm thick, 3.81 cm diameter pipe located at x=0 and z=3.175 cm 195

B.24 DGS for a 1.27 cm diameter pit in a .318 cm thick, 3.81 cm diameter pipe located at x = 0 and z= 3.18 cm 196

B.25 DGS for a 0.635 cm wide gouge in a .318 cm thick, 3.81 cm diameter pipe located at x=0 and z = 3.18 cm 197

B.26 DGS for a 1.27 cm diameter pit in a .318 cm thick, 3.81 cm diameter pipe located at x=1.27 cm and z=1.91 cm 198

B.27 DGS for a .635 cm diameter pit in a .318 cm thick, 3.81 cm diameter pipe located at x=.635 cm, z= 3.175 cm 199

B.28 DGS for a .635 cm diameter pit in a .318 cm thick, 3.81 cm diameter pipe located at x = .1762 cm and z = 2.92 cm 200

B.29 DGS for a 1.27 cm diameter pit in a .318 cm thick, 3.81 cm diameter pipe located at x = 0 and z = 3.18 cm 201

B.30 DGS for a .635 cm diameter gouge in a 0.318 cm thick, 3.81 cm diameter pipe located at x = 0 and z = 3.18 cm 202

Abstract of Dissertation Presented to the Graduate School
of the University of Florida in Partial Fulfillment of the
Requirements for the Degree of Doctor of Philosophy

NON-DESTRUCTIVE TESTING OF MATERIALS WITH THE DIFFERENTIAL GAMMA SCATTERING SPECTROSCOPY (DGSS) TECHNIQUE

By

Larry L. Humphries

May, 1989

Chairman: Dr. Samim Anghaie
Major Department: Nuclear Engineering Sciences

The Differential Gamma Scattering Spectroscopy (DGSS) technique is a novel means of non-destructive testing using Compton scattering to determine local density perturbations in a test sample. A test sample is irradiated with a narrow collimated beam of gamma-rays and the scattered radiation field is detected in a transversely placed high purity germanium detector. This detector provides excellent energy resolution so that a detailed energy spectrum can be obtained. This spectrum is then subtracted from a reference spectrum that was collected from a well-known, unflawed sample to obtain the differential spectrum. This differential spectrum contains all information characterizing the flaw. Using the relationship between scattering angle and scattering energy which characterizes

Compton scattering, the single scattered spectrum can be used to determine the location of scattering and, consequently, the density distribution along the portion of the primary beam path that passes through the sample.

A prominent feature of this study that distinguishes it from other Compton scattering research is the examination of the ability to detect flaws both on and off the primary beam path. A series of experiments was conducted to assess the sensitivity of the technique for detecting different sizes of flaws located throughout the sample. The results of these experiments are explained in terms of scattering events that lead to the differential spectra. With the experimental setup used in this report, it was possible to detect flaws as small as 0.1 cm in a solid 2.5 cm diameter aluminum rod both on and off the primary beam path. However, the experiment can be optimized by improved sources and detectors. It was not an objective of this report to determine the ultimate spatial resolution possible.

Processes governing the scatter of radiation in materials are well described by transport theory providing a strong theoretical foundation. It is thereby possible to calculate the probability that a measured differential spectra indicates the presence of a flaw. This ability provides a measure of reliability and determination of the flaw's presence is based on theory, not on operator experience.

CHAPTER1
INTRODUCTION

The Differential Gamma Scattering Spectroscopy (DGSS) technique is a means of detecting, sizing, and locating density perturbations in a test sample with respect to a reference state. An uncollimated detector measures the energy spectrum of the scattered radiation field from an unflawed object that is irradiated by a collimated, monoenergetic source of gamma radiation. This spectrum is saved and constitutes the reference spectrum. A test specimen is then examined by the detector in the same manner to obtain the test spectrum. When this spectrum is subtracted from the reference spectrum the differential spectrum results. This differential spectrum contains mostly information characterizing the density perturbation so that it is reasonable to expect that this differential spectrum may be analyzed to determine the location, size, or existence of a flaw in the test specimen.

An important feature of the differential spectrum developed throughout this paper is the fact that with this technique, flaws that do not lie on the illuminated chord can be detected. This paper analyzes this capability in terms of the photon interactions that lead to the differential spectrum. A sensitivity study demonstrates how the size of the flaw and location of the flaw in the test sample with respect to the detector affects the ability of the probe for flaw detection.

The DGSS technique is a recent development in an area of nondestructive methods investigated throughout the past three decades that is based on the measurement and analysis of the scattered photon field from a test object. This area of investigation is a departure from conventional industrial radiographic techniques where testing is based on measurements of the transmission of the incident gamma field. A short historical background of Compton scattering techniques would be useful at this point.

Early efforts were focussed on determining the electron density in a small inspection volume defined by a narrow collimated beam and the view field from a highly collimated detector [1]. The detector is collimated so that the multiple scattering component incident on the detector is reduced. If multiple scattering is negligible, the problem of calculating the average local volume is more straightforward. To obtain density information throughout the test object, it is necessary to move the object in relation to the detector and source so that the entire object can be scanned. This technique has been applied to both medical tomography and to nondestructive testing [2,3].

This technique has been expanded by using uncollimated detectors. Such detectors could then view the entire primary beam path through the test object. An uncollimated detector must be capable of high energy resolution if the density distribution along this path is desired. Then the measured energy spectrum, together with the relationship between scattering angle and scattering energy provide a kind of "energy collimation" of the detector. It is possible to correct for multiple scattering in the detector by analytically decomposing the scattered flux into orders-of-scattering components. Anghaie [4] has presented an iterative scheme for making such a correction.

The central contribution of this research to the advancement of radiation scattering methods is the analysis of the capabilities of the DGSS technique for detecting flaws off the illuminated chord. No previous work has investigated this potential of Compton scattering methods. The differential spectra are explained in terms of the photon interactions that occur within the region of the flaw and within the detector. Flaws along the primary beam path are primarily detected by single scattered photons that scatter directly from the flaw into the detector. Flaws located off the primary beam path are detected either by photons that undergo at least one scattering event in the flaw location, later interacting in the detector, or by a reduction of attenuation by photons passing through the flaw location into the detector.

Other methods of non-destructive examination are discussed in Chapter 2. A general description of ultrasonic testing, radiation scattering methods, infrared thermography, and eddy current testing together with some of the limitations of such methods are described so that the DGSS technique can be better understood in the context of conventional NDE techniques. The principles of the DGSS technique are detailed in Chapter 3. A general description of the technique in terms of single scattering and multiple interactions is presented and equations to calculate the differential spectrum are developed. In Chapter 4, inverse transport methods are discussed. A method for determining the location of a flaw along the illuminated chord from the measured differential spectrum is described. Chapter 5 discusses methods for correcting data for Compton broadening. It also contains a statistical analysis of differential spectra that is used to determine the statistical significance of a measurement of the differential spectrum and it describes changes in experimental parameters that can improve the statistics of a measurement. The experimental design is presented in Chapter 6. The gamma source, collimator, test sample, detector, detector response, and detector position are all described. Chapter 7 contains an analysis of the DGSS probe's abilities for detecting, locating, and sizing flaws in view of experimental measurements. Results of the sensitivity studies for solid rods and pipes are evaluated. Finally, Chapter 8 summarizes the results of this study, outlines some of the limitations of the method, and suggests areas for future improvement.

CHAPTER 2
NON-DESTRUCTIVE EXAMINATION BACKGROUND

Non-destructive testing (NDT) has become an integral tool of modern industry. Safety concerns, plant reliability and quality control have all placed demands on our ability to probe the surface of structural components, equipment and industrial materials. Nuclear power is one field in particular that has seen the value of NDT for pre-service and in-service inspection to monitor the quality and integrity of reactor components, to ensure the safe operation of reactors and to verify compliance with federal regulations. Aside from the obvious benefits of safe operation, there is also a monetary benefit realized by improved plant reliability. One study on piping reliability has estimated that NDT can save a pressurized water reactor $20 million over the lifetime of the plant due to fewer "false call" replacements of acceptable components [5]. It estimates that for a boiling water reactor the savings due to in-service inspection from a reduction of pipe leaks may be as high as $8 to $144 million.

For an NDT technique to be accepted by industry it must demonstrate its ability to detect, size and locate flaws in a variety of material applications. In addition it must provide sufficient spatial resolution, high reliability, and rapid processing speeds. By way of example, in testing boiler tubes where wall thinning, pitting, and cracking can occur, linear scan rates of 15.2 m/min are desired. Of course these design considerations will vary with application.

In order to meet these needs a variety of techniques have been developed making use of a number of natural phenomenon. Examples of such phenomenon are the scattering of sound waves from surfaces in ultrasonic testing, the interaction of radiation in radiography, the uneven conduction of heat around discontinuities and the resulting non-uniform transient temperature distribution used in infrared imaging, and the distortion of eddy currents by surface cracks. It is the purpose of this chapter to discuss some of the more prevalent NDT methods, their benefits and limitations so that the current technological context of NDT is better understood.

Ultrasonic Testing

Ultrasonic testing is perhaps the most widely used technique today. It has been successfully applied to detection of flaws in heavy piping, light tubing, heavy forgings, and some castings. In addition to metals, flaws can be detected in concrete, wood, rubber, plastics, organics, ceramics, and glass.

The basic phenomenon employed in ultrasonic testing is the transmission, scattering, and reflection of sound waves in materials [6,7,8]. There are several modes by which sound can propagate throughout the medium of which two fundamental waves are frequently used: longitudinal and transverse waves. Longitudinal wave oscillations occur in the direction of propagation as in Figure 1a. This periodic variation in states of compression and rarefaction is the means by which sound is transmitted in air. In solids, a transverse oscillation perpendicular to the direction of propagation can occur (see Figure 1b). Because of the state of shear which exists, these are also called shear waves. There are other waves that exist which can be recognized as superpositions of the fundamental waves together with reflected and refracted waves. These include Rayleigh waves, Lamb waves, Love waves, and rod waves. The transmission, reflection, and dispersion properties of a material will vary for these different wave forms. Use can be made of this fact for selection of the proper wave form best suited for a particular application. For example in steel a 2 MHz longitudinal wave has a wavelength of 3 mm (speed of sound = 5.9 km/s, since the product of frequency and wavelength is the sound speed). However, a transverse wave has a wavelength of 1.6 mm (speed of sound = 3.2 km/s). Since a wave is able to detect flaws on the order of the

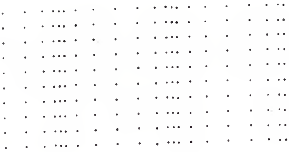

a) Longitudinal

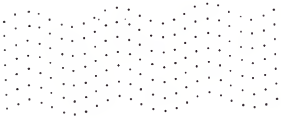

b) Transverse

Figure 1. Ideal ultrasonic wave oscillations

wavelength, transverse waves are slower yet more sensitive to smaller defects.

The two most common methods employed in ultrasonic testing are intensity and pulse-echo methods. In the intensity method a detector measures the transmitted signal which is attenuated by the path length separating the source and the detector. If a flaw lies along the path length, the resulting shadow will appear as a reduction in the measured intensity of the detector. In the pulse-echo method, a sound pulse is delivered by a transmitter and the receiver records the time varying reflected signal. The time at which a pulse arrives at the detector is an indication of the distance travelled by the pulse. This is the same concept behind sonar and radar.

When sound waves reach a boundary between two material regions, the wave will be partially reflected and transmitted depending on the angle of incidence of the incoming wave and the acoustic properties of the two materials. This interaction is complicated by the effects of refraction and the superposition of incoming and outgoing wave forms. Unless the material region borders on a vacuum, the intensity of the reflected beam is less than that of the incident beam. Since many of the ultrasonic techniques are based on the reflection of the sound waves from flaws, there is necessarily a loss in signal intensity when comparing the measured signal to the transmitted signal.

In addition, there are other signal losses due to attenuation in the material. Attenuation comprises both scattering and absorption. Absorption is the process by which a sound wave is converted into heat due to a kind of "friction" from the particle oscillations. Scattering is the process in which a sound wave may interact with pores, grain structures, inclusions, or other inhomogeneities. The degree of attenuation due to scattering increases with the size of the inhomogeneity or with anisotropy. Both absorption and scattering increase with frequency. By going to lower frequencies, it is possible to reduce attenuation but this tends to also increase the wavelength thereby reducing the sensitivity of the method. Absorption can be corrected for by increasing the intensity of the source, but this corrective measure may not be effective in counterbalancing the scattering term since an increased level of noise due to scattered waves may mask significant signals.

The pressure of a transmitted signal drops off exponentially because of material attenuation, characterized by the material attenuation coefficient, α. When combined with the geometric attenuation, the pressure, p, at a distance, A, from a probe generating spherical waves in an infinite medium is $p = p_0 \cdot \pi \cdot N/A \cdot \exp(-\alpha A)$.

Attenuation in materials, characterized by the attenuation coefficient, α, can limit the size of the object that can be tested. For $\alpha < 10$, as is expected from light metals, fine grained steels, cast aluminum, worked steel, aluminum, and magnesium, samples can range from 1 to 10 m. Also, for $10 < \alpha < 100$, such as is expected for some plastics, cast aluminum, alloyed metals, worked copper, and zinc, samples can range from 0.1 to 1 m. Objects made of plastics, rubber, wood, cast steels, highly alloyed metals, cast copper, zinc, brass, and porous ceramics which all have $\alpha > 100$ are limited to samples smaller than 0.1 m. Composite materials generally cannot be studied by ultrasonic transmission.

There are several problems that arise in ultrasonic testing that complicate existing procedures. When using the pulse-echo methods, large obliquely oriented flaws may not be detected unless the detector is properly oriented to intercept the reflected pulse. Also large surface discontinuities will mask small flaws which lay in their shadows. The acoustic coupling between the probe and sample can critically affect the ability to use ultrasonic methods. Commonly, sound waves are generated in a piezoelectric probe and must be transferred to the test sample. A rough or dirty surface will result in incomplete contact and either a weak or aberrant signal will result. A roughness of more than 1/10 the wavelength or an uneven surface with irregularities as large as the probe will compromise the coupling. To remedy this the surface must be carefully prepared by grinding, sanding, and cleaning. This process may be time consuming or expensive and it may not be possible to obtain good contact coupling if the object has extremely complicated surface features. Instead coupling media such as immersion testing may be necessary or the sound wave can be generated electromagnetically in the outer surface of a metal sample (so-called EMAT devices) so that acoustic coupling is not necessary.

Radiation Scattering Methods

Radiation scattering can be utilized in NDT systems to detect fluctuations in material density as would be expected from cracks or inclusions. Radiation from a laboratory source (neutrons and gamma-rays are most conveniently used because of their electrical neutrality) can be collimated into a parallel beam and strike a test sample. A detector must then be used to measure either the intensity of the unscattered radiation, the intensity of the scattered radiation, or the energy spectrum of the scattered radiation. The information present in the detector observations must then be processed to deduce flaw location and size. Unlike ultrasonic waves, gamma-rays are not grossly reflected by discontinuous density fluctuation such as interfaces. In ultrasonic NDT tests, deep flaws or cracks may be masked by surface flaws or by other material discontinuities. Gamma-rays are not affected significantly by surface effects but are scattered rather continuously throughout the material on a volumetric basis. However, this continuous attenuation may pose a limitation on the depth at which flaws can be detected as the beam may be reduced to undesirably low levels in thick samples.

Another difficulty posed by radiation scattering techniques may lie in the ability to analyze the information observed by the detector to obtain information about the density variation. In all but the simplest techniques, the information observed is only indirectly related to the size and location of the flaw. The mathematics relating measured quantities and physical flaw location are not altogether straightforward.

Gamma-rays are generated in the radioactive decay of some nuclei. They appear following a precursor decay process such as beta decay. For example, Co-60 decays by producing a beta particle (an energetic electron), followed by the emission of a gamma ray necessary for the product nuclei to obtain lower energy states. They are electromagnetic radiation, not unlike light rays, ultra-violet rays, or x-rays; they are visualized as electrically neutral photons that can interact with matter as particles. Because gamma-rays carry off the large energies from nuclear transitions, they generally have energies much greater than other forms of EM radiation. For example, Co-60 gamma rays have energies of 1173 or 1332 keV compared to 100 to 300 keV typical of x-rays, or 2 or 3 eV typical of light rays.

A photon passing through a material can interact with that material. A significant interaction mechanism in the energy range 50 keV to 1000 keV is that of Compton scattering, i.e. a scattering interaction that takes place between a photon and an electron in the medium. A photon will be scattered by an electron and leave with angle Θ (see Figure 2). In any one particular interaction one cannot predict what that angle will be but one can, however, describe the probability distribution $f(\Theta)d\Theta$ for a photon emerging with angle Θ in $d\Theta$. A quantity closely related to the probability distribution that is frequently used in radiative transport calculations is the differential scattering cross-section, $\sigma(\Theta)$. For a collimated beam incident on a volume element dV, the two are related by

$$p_V\, f(\Theta)d\Theta = 2\pi\, \sigma(\Theta)d\Theta \;\frac{Z_n N_0}{M}\, dV \qquad [1]$$

where p_V is the probability an incident photon interacts in volume element dV, Z_n is the number of electrons/atom, N_o is Avogadro's number, and M is the molecular weight of the medium. Note that scattering at any angle increases with Z_n. This suggests that since scattering increases with material density Compton scattering might be useful in determining density variations. The Klein-Nishina formula [9] for the differential cross-section is

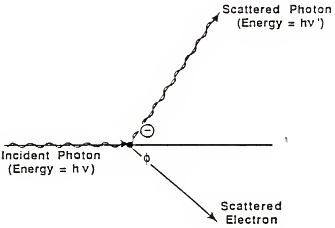

Figure 2. Photon-electron scattering interaction

$$\sigma(\Theta) = r_o^2\left[\frac{1}{1+\alpha(1-\cos\Theta)}\right]^3\left[\frac{1+\cos^2\Theta}{2}\right]\left[1+\frac{\alpha^2(1-\cos\Theta)^2}{(1+\cos^2\Theta)(1+\alpha(1-\cos\Theta))}\right] \qquad [2]$$

where $\alpha = E_o/511(\text{kev})$ and r_o is the classical electron radius. Figure 3 shows a plot of $\sigma(\Theta)$ for several incident energies, Eo.

Another cross-section that frequently appears is the total Compton scattering cross-section, σ_s. This is obtained by integrating the differential cross-section over all angles, $\sigma_s = 2\pi \int_0^{\pi} \sigma(\Theta)d\Theta$.

A simple approach to Compton scattering NDT is shown in Figure 4. If a collimated source and collimated point detector are placed apart with a sample located between them, the detector will observe only those gamma rays that have not scattered in the sample:

$$I = I_o \exp\left(-\int_0^D \sigma_s \frac{\rho(x)\ N_o Z_n}{M} dx\right) \qquad [3]$$

where I_0 is the total source strength (gammas/sec), I is the detection rate (gammas/sec), $\rho(x)$ is the density of the sample at position x, σ_s is the total scattering cross-section, M is the molecular weight, D is the length of the illuminated chord, and N_0 is avogadro's number. Note that, in this example, if a flaw lies along the illuminated chord length, this will effect the intensity observed by the detector. If the flaw has the effect of decreasing the

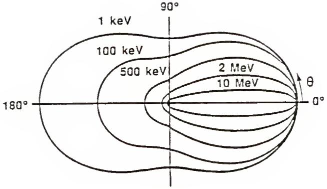

Figure 3. Polar plot of the Klein-Nishina formula for the Compton cross-section

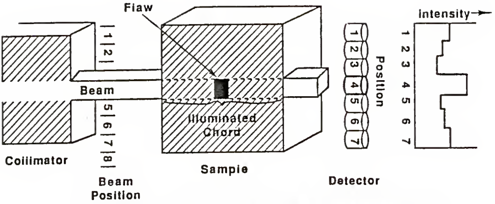

a. Beam and detector scans sample to determine average density in illuminated chord.

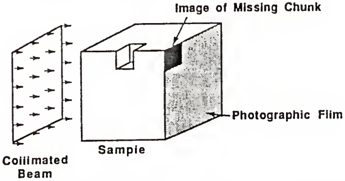

b. Radiography is a simple example of compton scattering NDT

Figure 4. Compton scattering NDE techniques

local density at some location along this path (a crack or hole), the detection rate will increase.

This basic idea is the principle behind radiography [10]. In the case of radiography, the collimated beam may be quite wide exposing the entire sample and the detector is a sheet of film (a sheet of film can be thought of as a large collection of small point detectors). If a flaw has the effect of increasing the local density at some location along the path of the beam, the film will be exposed to less radiation and will appear darker, forming an image of the flaw profile. Notice that unless a radiograph is performed at more than one angle, the best one can hope for is a shadow of any flaw present and one would not be capable of determining the flaw location in three dimensions.

Another possible test system is shown in Figure 5a. Here a number of collimated beams are passed through a sample and the intensity of the attenuated uncollided beam is measured as the beam emerges from the other side. From equation 3, the chordal average density of the material can be calculated for each pass through the sample. If several passes are made through a grid of pixels, it may be possible to detect locations of flaws locally throughout the sample. If an unflawed sample consists of a uniform density distribution, those beams that pass through flaws will yield intensity measurements which differ from those calculated from theory. As shown in Figures 5b, 5c, and 5d it may or may not be possible to determine the precise location of the

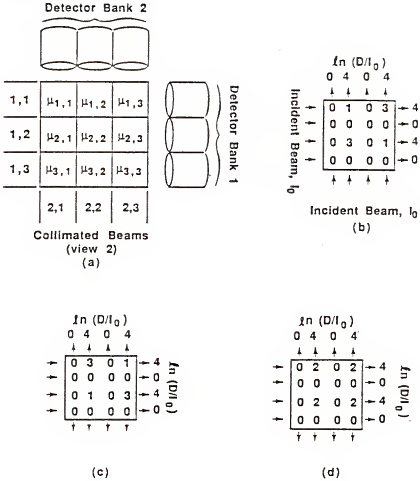

Figure 5. Computerized axial tomography.
a) Detector/beam configurations, b), c), d) Three material density profiles that give the same detector response.

flaw or the flaw size as there are only 8 equations for the 16 unknowns. In this particular example the problem is not well-defined and unique solutions will not result.

Computerized axial tomography (CAT) [11,12] utilizes Compton scattering in order to construct a 2- or 3-dimensional density distribution. As explained above, more than 1 or 2 view angles are needed to obtain pictures with 2- dimensional information and reasonable resolution. The sample to be analyzed is divided into a number of pixels as seen in Figure 6. The density of each pixel is assumed to be uniform so that the resolution is of the order of pixel size. As is seen in the figure, a number of beams are passed through the sample and detectors are situated to detect the uncollided intensity. When the beam is directed at 0° and 90° as shown in the figure, it passes through one row or 1 column and no other pixels. However, at intermediate angles, it passes through fractions of pixels. Now it becomes necessary to account for these fractional areas. The equations

$$I_{ij} = Io_{ij} \exp\{- \sum_{ij}(\mu_{ij} w_{ij})\} \qquad [4]$$

form a matrix system. All the material properties of pixel i,j are incorporated into the definition of μ_{ij}, where $\mu_{ij} = \sigma_{ij} \rho_{ij} N_0/M_{ij}$, and the geometrical weighting factor is included in w_{ij}. A large number of views may be taken at intermediate angles so that additional equations result

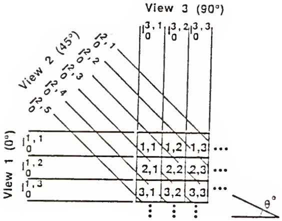

a) Intermediate view angles

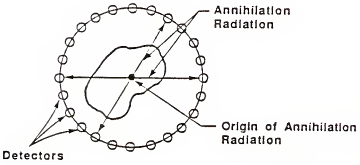

b) Positron emission.

Figure 6. Computerized axial tomography scan.

and unique solution may be possible for large arrays of pixels. The system of equations can be inverted using a variety of techniques. The matrices involved can be quite large and certain techniques can offer savings in computer time or storage requirements over others.

There are several variations in tomography. In some biological cases the patient can be given radioactive tracer elements that isolate in certain organs. In this case the source is internal rather than external. If the radioisotope is a positron emitter, the positron will annihilate with an electron and emit two photons of equal energy and traveling in opposite directions. If two detectors among a large bank of detectors surrounding the patient detect annihilation radiation at nearly the same time, the annihilation took place somewhere along the line joining them.

Radiography and conventional computerized axial tomography are based on measuring the transmission of photons through the test material. A single measurement, whether it be through exposure of film or detection of photons in a properly collimated detector, provides only an estimate of the average material density along the path of the incident source beam. To obtain a distribution along the incident beam path, it is necessary to scan the object from various views.

Other techniques are based on measurement of the scattered radiation field [1, 2, 3, 4, 13, 14, 15]. The inverse problem of determining the density profile from the scattered energy spectrum is possible because of a well defined relationship between scattering angle and energy after scatter. These techniques have focussed on the single scattered spectrum for flaw detection. Various refinements of this technique have achieved success in the measurement of local densities.

Infrared Thermography

All objects with temperatures above absolute zero emit thermal radiation to their surroundings. This radiation is described by

$$I = \epsilon_o \, \sigma_s \, T_o^4 \qquad [5]$$

where I = intensity (power / unit area)

ϵ_o = emissivity

σ_s = Stefan Boltzmann constant

T_o = surface temperature of object

There is also a transfer of energy from the surroundings to the object so that the net energy emitted by the object is

$$I = (\epsilon_o T_o^4 - \alpha_o \, \epsilon_s \, T_s^4)\sigma_s \qquad [6]$$

where s refers to the surroundings, o refers to the object, and alpha refers to the absorptivity.

The temperature distribution on the surface of a sample is affected by the appearance of flaws [16]. This is seen in examining the heat conduction equation without internal heat generation.

$$\cdot(k\ T) = \rho c_p \frac{\delta T}{\delta t} \qquad [7]$$

For steady state and uniform, isotropic conduction, the solution for the surface temperature Ts on an infinite cylinder with inner wall temperature Ti, and ambient temperature T is given by

$$\frac{T_s(r_2)-T_i}{T_\infty - T_i} = \frac{R_1}{R_T} = \Theta(r_2)$$

$$R_1 = h\ \left(\frac{R_2/r_1}{2\pi h} \right)$$

$$R_T = R_1 + \frac{1}{2\pi r_2 h} \qquad [8]$$

where r_1, r_2 are the inner and outer wall radii, respectively, and h is the convection coefficient.

As r_2 decreases, the surface temperature approaches that of the inner wall temperature. This may be the case for a boiler tube that has thinned due to corrosion or wear. If r_n is the nominal radius of the tube then the percent change from the nominal surface temperature is given by

$$\frac{T_s(r_2) - T_s(r_n)}{T(r_n)} = \frac{\Theta(r_2) - \Theta(r_n)}{\Theta(r_n) + T_i/(T_\infty - T_i)} \qquad [9]$$

Heat removal from the outer surface is frequently inefficient so that $\Theta(r_2) \approx \Theta(r_n) \approx 1$. In this case the percent change from the nominal temperature is so small it becomes difficult to detect. To overcome this apparent impasse, it is necessary rather to monitor the transient temperature distribution. Here thinner regions will transfer heat faster and hence temperatures will reach equilibrium values sooner. In the case of boiler tubes the experimental objective is to rapidly establish an initial temperature difference between the inner and outer wall along the entire length of the tubes. Two methods have been proposed to accomplish this. First, high temperature water under high pressure can be forced into the mud drum of the boiler and is allowed to flash to steam at the lower pressure inside the tubes. This would yield a convenient initial condition where the inner wall is subjected to a uniform constant temperature of 212°F. The second approach is to maintain a constant high temperature to the tube feedwater. The outer surface is rapidly sprayed with cool water and the transients are watched. Of course, these two methods are merely variations of the same idea.

Modern technology has achieved infrared detectors capable of sensitive temperature measurements of about one hundredth of a degree Fahrenheit. Furthermore, these detectors are able to focus on very small points at the surface of an object and can rapidly scan the entire object. This ability to rapidly scan a surface makes IR an attractive means of testing a sample with a large surface area. For example, in testing boiler tubes, IR was able to detect flaws as small as 25% of the wall thickness at a rate of 20 m/min However, IR does not provide the resolution offered by other techniques.

Eddy Current Testing

An alternating current applied to a coil generates a field of magnetic flux lines at the center of the coil. The direction of the lines of flux are as shown in Figure 7. If an electrically conductive material passes through this magnetic field, continuous and closed eddy currents are induced in the material such that they generate an opposing magnetic field which tends to weaken the primary magnetic field. This weakening is described in terms of an increase in the complex impedance of the coil. Discontinuities in the electrically conductive material due to flaws will cause these eddy currents to be distorted from their natural path [10, 17]. This tends to reduce the opposing magnetic field and thereby increase the coil impedance.

Figure 7a shows two methods of eddy current testing. In Figure 7a, the coil is mounted on the surface of the test specimen so that the magnetic field is directed into the sample. The probe scans the surface of the sample and the impedance is recorded and analyzed for flaw detection. The separation distance A is an important factor since the impedance depends sensitively on it. When phase and

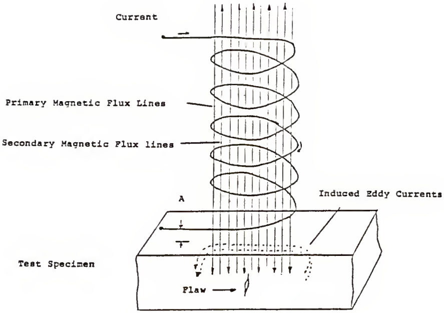

a) Surface mounted probe

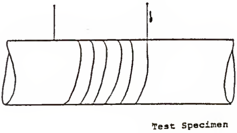

b) Enveloping probe.

Figure 7. Eddy current probe

magnitude are both monitored, it is possible to distinguish between changes in impedance due to variations in A from changes due to flaws. It is also possible to distinguish these two effects by connecting two such probes in a differential arrangement such that their magnetic flux directions are antiparallel and comparing their two signals.

Figure 7b shows how the coil can completely encircle a sample such as a tube. Again eddy currents are generated so that their induced magnetic flux opposes the magnetic flux of the coil inside the material and the observance of a change in complex impedance can be related to the occurrence of flaws.

Eddy current tests are limited to detection of surface flaws or examination of thin metal components. The skin depth which is an indication of the penetration depth is given by

$$\delta = 2 \times 10^{3} \quad (f\ \mu\ \sigma)^{1/2} \qquad [10]$$

δ = skin depth (inches)

f = frequency (Hz)

σ = electrical conductivity $(\text{ohm-cm})^{-1}$

μ = magnetic permeability

It would seem that it might be possible to go to deeper penetration depths by decreasing the frequency. However this is not practical because at such low frequencies it is difficult to discriminate changes in impedance due to flaws from changes due to lift-off and because sensitivity is also compromised.

CHAPTER 3
DIFFERENTIAL GAMMA SCATTERING SPECTROSCOPY METHODS

The Differential Gamma Scattering Spectrum (DGSS) technique was suggested as early as 1984 by Anghaie and others [18, 19, 20, 21]. Studies conducted by Anghaie have demonstrated the feasibility of the DGSS technique for flaw detection. Cracks and holes as small as 1 mm in diameter have been detected with this technique. In addition, it was observed that flaws located in regions off the primary beam path could also be detected with this technique.

The DGSS technique acquires its name from the practice of subtracting the spectrum obtained by scattered radiation from a test sample to that spectrum obtained from a reference sample. The information that is obtained from this differential spectrum is indirectly related to the variation in physical properties between the test and reference sample. In particular, density variations resulting from cracks or flaws will yield a differential spectrum. The differential spectrum can then be analyzed and mathematically manipulated (the problem can be inverted) to determine the variations in the physical properties.

The basic principles in DGSS can best be examined through investigation of a simple experiment. Consider the detector of Figure 8. The surface of the detector is placed a distance x away from a parallel beam of gamma-rays. Since the beam is parallel to the surface, when there is no material along its path, the detector will observe no gamma-rays. However, if a sample of length dz is placed in its path, photons will scatter from the sample to the detector. If only those photons that scatter once in the sample are considered, the radiation field incident on the detector is described by

$$N(\Theta)d\Theta = I_o\ A_o\ \frac{\rho N_o Z_n}{M}\ \sigma(\Theta)d\Theta\ \delta\phi\ dz \qquad [11]$$

where $\Theta \in \{\Theta_{min}(z),\ \Theta_{max}(z)\}$

$N(\Theta)d\Theta$ = the number of gamma-rays that scatter from the sample with angle Θ into the detector

I_o = the number of gamma-rays in the collimated beam ($cm^{-2}\ sec^{-1}$)

A_0 = area of beam

Z_n = number of electrons/atom in sample

N_0 = Avogadro's number

M = molecular weight of sample (g/mole)

ρ = density of sample (g/cc)

$\sigma(\Theta)$ = microscopic cross-section for scattering an angle of Θ per electron (cm^2)

$\delta\phi$ = the azimuthal angle subtended by the detector

As shown in the figure, the detector subtends polar angles ranging from Θ_{min} to Θ_{max} for each pixel location. The microscopic cross-section, $\sigma(\Theta)$, which describes the polar

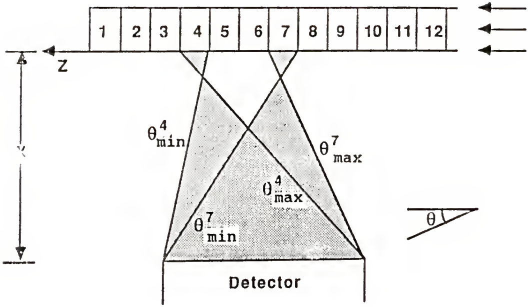

Figure 8. Variation of scattering angle with position of flaw along illuminated chord.

angular distribution of the scattered photons can be calculate from the Klein-Nishina formula (see equation 5). The probability density for the azimuthal angle is uniform and the energy after scattering is independent of the azimuthal angle. Since the detector measures the energy distribution of scattered photons, the measured detector response is determined by the polar angular distribution which is a function of the Klein-Nishina formula together with the azimuthal angle intercepted by the detector. Notice that the spectrum observed by a sample at location 7 differs from that observed for location 4 since the detector intercepts different scattering angles. As the flaw is moved from left to right in the diagram, the scattered spectrum will shift to higher energies. Thus, the shape and position of the differential spectrum indicates the flaw size and location.

Now consider the detector of Figure 9a. Here, the reference sample consists of a solid of uniform density. The observed angular distribution of the single scattered spectrum is given by the integral

$$N_1(\Theta)\,d\Theta = \frac{I_o A_o Z_n N_o}{M} \int_0^D [\rho_r(z) e^{-\mu z}\ e^{-\mu' z'}\ \sigma(\Theta)\, d\Omega]\, dz \qquad [12]$$

where μ,z and μ',z' are the attenuation coefficients and distances travelled in the medium before and after scattering respectively and D is the length of the illuminated chord.

a) Reference

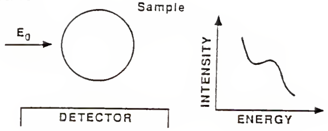

b) Test Sample (with holein center)

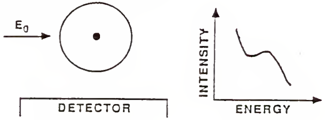

c) Difference

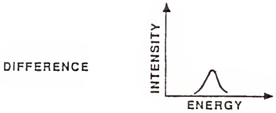

d) Material located at center

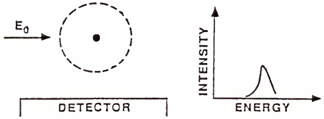

Figure 9. Definition of differential spectrum

Also consider a test sample that is almost identical to the reference sample, except for a density perturbation at pixel k. The observed angular distribution for this case is given by the integral

$$N_2(\Theta)d\Theta = \frac{I_oA_oZ_nN_o}{M} \int_0^D [\rho_t(z)e^{-\mu z}\ e^{-\mu' z'}\ \sigma(\Theta)d\Omega]dz \qquad [13]$$

The difference between the two spectra

$$(N_1-N_2)(\Theta)d\Theta = \frac{I_oA_oZ_nN_o}{M}\ [\delta\rho_k(z)e^{-\mu z}\ e^{-\mu' z'}\ \sigma(\Theta)\delta\Omega\ \delta z] \qquad [14]$$

is approximately equivalent (if there were no multiple scattering) to the spectrum that results from the flaw at pixel k alone, reduced by an attenuation factor (see Figure 9c, 9d and equation 11).

The once-scattered spectra for a 0.25 cm hole located on the illuminated chord is shown in Figure 10 for three hole locations. This calculation was for a 2.5 cm diameter aluminum sample in which the illuminated chord passes through the sample center along the diameter and the detector is 1.8 cm from the illuminated chord, positioned such that its central axis is normal to the illuminated chord and intersects it at the sample center. It has not been corrected for the detector response. When the hole is located 0.625 cm from the point of incidence, photons may scatter with energies ranging from 210 keV to 550 keV. As the hole moves farther along the illuminated chord, low

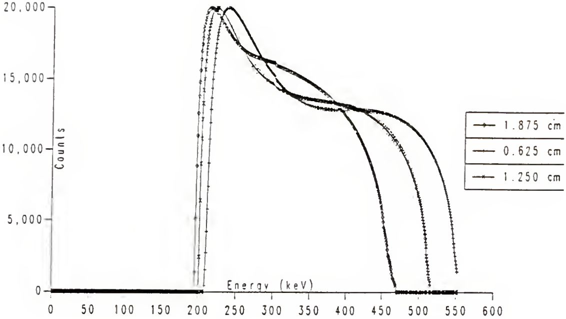

Figure 10. Ideal single scattered differential spectrum for a 0.25 cm hole located along the illuminated chord at three distances from point of beam entry.

angle (high energy) once-scattered photons no longer intercept the detector and the differential spectrum shifts to lower energies. This gives an idea as to how the Differential Gamma Spectrum, DGS, is determined by hole location and suggests that the inverse problem may be possible.

Multiple Interactions

We have attempted to separate the single scattered spectrum from the total spectrum since multiple interactions can complicate the mathematical analysis of the differential spectrum. As discussed in a following section positioning the detector to intercept lower angles of scatter can help reduce the overlap of single and multiple scattering. However, multiple interactions cannot be entirely eliminated through the DGSS method. In fact, there are practical reasons for retaining multiple interactions for the additional information it provides. As seen above, were it not for multiple interactions it would not be possible to detect flaws unless they are located along the illuminated chord since, when the source is a narrow collimated beam, all single scattering interactions take place there. A photon must interact more than once if it is to be possible to detect flaws not located on the illuminated chord.

To understand the contribution of multiple photon interactions in detecting flaws, look at the set of interactions that take place in the reference spectrum which don't occur in the flawed sample. Take for example the circular hole of Figure 11a. The set of all photons which undergo a scattering event in the reference test piece at the hole location will contribute to the reference spectrum and will be absent from the test sample spectrum.

Moreover, the existence of the hole will mean less attenuation in the flawed sample. As shown in Figure 11b, photons that scatter such that their path passes through the hole have a greater probability of passing through the sample to the detector without interacting again in the sample.

These two effects are opposing and explain the fact that the differential spectrum for flaws located between the detector and the illuminated chord varies from negative values at high energies to positive values at lower energies. At high energies, single scattered photons can pass directly through the hole location into the detector. Keeping in mind that the differential spectrum is defined as the reference spectrum minus the test specimen, since the detector viewing the test sample observes more photons (less attenuation), the differential spectrum will be negative. At lower energies multiple scattering dominates and the differential spectrum is positive.

Flaws located on the side of the sample opposite the illuminated chord will be detected almost entirely by

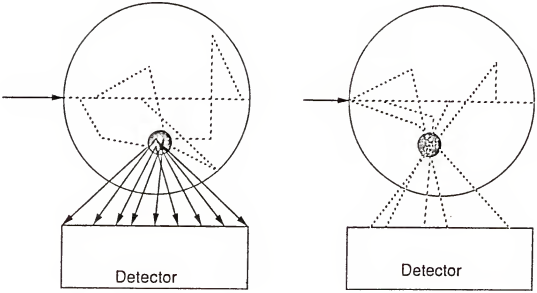

a) Scattering from flaw location

b) reduction in attenuation

Figure 11. Multiple scattering events contributing to the differential spectrum.

multiple scattering as a result of scattering events taking place in the flaw location. The differential spectrum (reference spectrum minus the sample spectrum) is positive for all energies. The intensity of this spectrum for such holes is much smaller than its counterpart reflected across the illuminated chord and such holes are more difficult to detect with one detector. This suggests that the sensitivity of the system can be improved by using two detectors placed on opposite sides of the illuminated chord.

The Direct Spectrum

The direct spectrum resulting from radiation scattered off the sample into the detector could be analyzed for flaw detection, location, and size. Figure 12 shows the measured direct spectrum corrected for the detector efficiency for a 0.25 cm centrally located hole in a 2.5 cm test piece. The spectrum shows a broad distribution, several narrow peaks, and abroad peak at the lower energy. The broad distribution is from scattering in the sample and background due mostly to insufficient shielding of the source. The narrow peaks correspond to Pb x-rays or Cs-137 gamma-rays. The broad lower energy peak is a component of background caused by back-scatter of the incident beam off the lab wall.

There are several advantages of analyzing the differential spectrum over the direct spectrum. First, background is automatically removed in calculating the

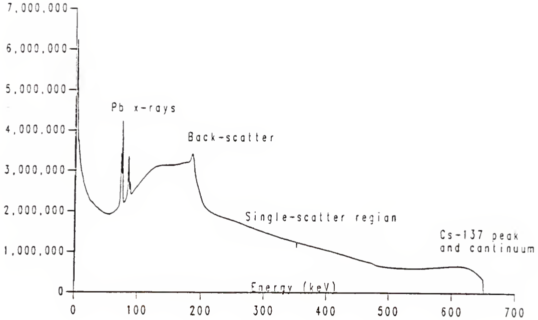

Figure 12. Direct scattering for a 2.5 cm sample.

differential spectrum. In a direct spectrum it is necessary to collect a spectrum with the test piece in place and then once again with the test piece removed. This second spectrum would constitute the background spectrum. This would not however remove all background events. Photons that interact with objects in the surrounding test area that then scatter into the test piece and into the detector would not be counted. However, this may or may not be significant depending on how well the source is shielded, the test piece size and the proximity of the object to surroundings.

Secondly, some of the multiple scattering is removed from the differential spectrum. The multiple scattering factor is defined as the ratio of all photons with energy E in dE which scatter after one or more collision into the detector to those photons that scatter only once into the detector. Figures 13 and 14 show the multiple scattering factor for the direct and the differential spectra respectively for the case of a 0.25 cm, centrally located hole in a 2.5 cm diameter test piece. The multiple scattering factor is a bit larger at lower energies in the case of the direct spectrum. However, over most of the range the two are indistinguishable. Notice that at high energies it approaches unity for both cases and the spectra do not depend sensitively on multiple scattering.

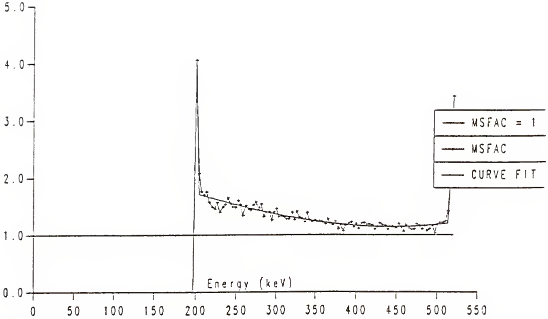

Figure 13. Multiple scattering factor for a differential spectrum from a 2.5 cm test piece with a 0.25 cm central hole.

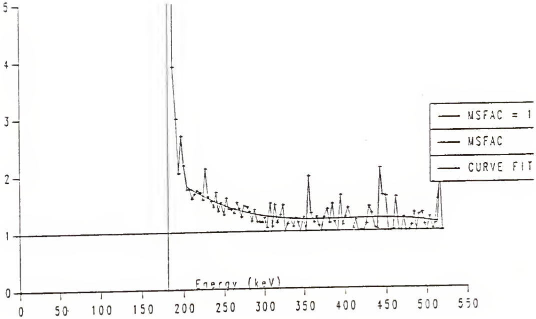

Figure 14. Multiple scattering factor for a direct spectrum from a 2.5 cm test piece with a 0.25 cm central hole.

Most importantly, only those events which occur as a result of the flaw appear in the spectrum so that a non-zero differential spectrum indicates the presence of a flaw. Particle tracks not passing through the flaw are eliminated so that one is looking only at essential information characterizing the hole. The amount of nonessential information in the direct spectrum can overwhelm the significant information it may contain. This is seen readily in Figure 15. This figure is the result of a Monte Carlo calculation of the direct spectrum for the flawed and unflawed samples. It shows the ratio of the number of counts in the direct sample due to photons passing through or interacting in the flaw to the total number of counts in the direct spectrum for the flawed test piece. At high energies this ratio goes to zero since photons scattering from the hole with such energies do not intercept the detector. In the range of energies corresponding to single scattering in the hole, the ratio rises to a fairly level plateau and then drops off at lower energies. This ratio is approximately 0.1 over most of the energy range which corresponds to the ratio of the hole diameter to cylinder diameter. If background were added, the differential spectrum is almost lost in the total spectrum.

Development of Transport Equations

Up until now we have restricted our attention to the single scattered spectrum. Now we will shift our focus to

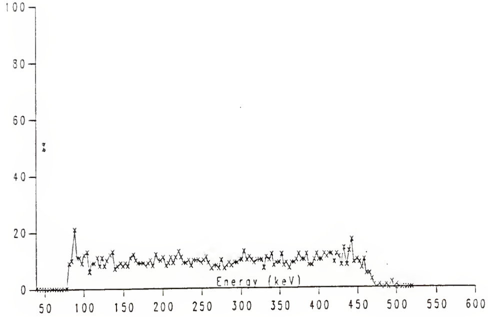

Figure 15. Ratio of calculated differential spectrum to direct spectrum for a 2.5 cm test piece with a 0.25 cm central hole.

developing equations for the total differential spectrum, including multiple scattering.

The detected spectrum, D(E), is determined by integrating the angular differential flux over the surface of the detector [22].

$$D(E) = \int_A dA \int_{2\pi} d\Omega \int_0^{E_o} R(\underline{r},\underline{\Omega},E',E)\phi(\underline{r},\underline{\Omega},E')dE' \qquad [15]$$

where A is the coaxial detector effective area, $\phi(\underline{r},\underline{\Omega},E)$ is the photon flux, and $R(\underline{r},\underline{\Omega},E',E)$ is the detector response function or the probability that a photon at $\underline{r}$, traveling in direction $\underline{\Omega}$ with energy E' is counted in the detector channel corresponding to energy E.

The photon flux can be separated into an infinite sum of partial fluxes, $\phi^{(n)}$ [4,23]:

$$\phi(\underline{r},\underline{\Omega},E) = \sum_{n=0}^{\infty} \phi^{(n)}(\underline{r},\underline{\Omega},E) \qquad [16]$$

where $\phi^{(n)}$ represents the contribution to the total flux due to photons suffering n scatter events.

Inserting the sum into equation 15, the detected spectrum becomes

$$D(E) = \int_0^{E_o} dE' \int_A dA \int_{\Omega} d\underline{\Omega}\, R(\underline{r},\underline{\Omega},E',E) \sum_{n=0}^{\infty} \phi^{(n)}(\underline{r},\underline{\Omega},E') \qquad [17]$$

$$= \int_0^{E_o} R_2(E',E)[j^{(0)}(E') + j^{(1)}(E') + \ldots]\ dE'$$

where

$$j^{(n)}(E) = \frac{\int dA \int d\Omega \; R(\underline{r},\underline{\Omega},E,E')\phi^{(n)}(\underline{r},\underline{\Omega},E)}{R_2(E,E')} \qquad [18]$$

is the total number of nth collided photons with energy E which are counted by the detector. $R_2(E,E')$ is the probability that a photon with energy E is counted as having energy E'. Since the incident beam does not pass through the detector, $j^{(0)} = 0$.

What we have calculated here is the direct scattering spectrum. To obtain the differential spectrum we take the difference between the detected reference spectrum and the flawed sample spectrum.

$$D(E) = D_{ref}(E) - D_{samp}(E) \qquad [19]$$

$$= \int_0^{E_o} [((j_{ref}^{(1)}-j_{samp}^{(1)})+(j_{ref}^{(2)}-j_{samp}^{(2)}+\ldots)] \; R_2(E',E) \; dE'$$

This equation involves an infinite sum of terms which represent the contribution to the total spectrum due to n-collided photons. It can be manipulated into a form which allows calculation of the detector response in terms of the single scattered spectrum described above and the multiple scattering factor

$$D(E) = \int_0^{E_o} dE' \; R_2(E',E)[j_{ref}^{(1)}(E') \; B_{ref}(E')-j_{samp}^{(2)}(E') \; B_{samp}(E')] \qquad [20]$$

where $B(E)$ = the multiple scattering factor

$$= [j^{(1)}(E) + j^{(2)}(E) + \ldots] \; / \; j^{(1)}(E) \qquad [21]$$

and $E \in$ {Energy range of single scattered photons}

From earlier discussion, it is possible to calculate the single scattered spectrum measured by the detector from the density profile, þ(z).

$$j^{(1)}(E) = \frac{I_o A_o Z_n N_o/M}{R_2(E,E')} \int_A dA \int_{\Omega_{det}} d\Omega \int_0^D R(\underline{r},\underline{\Omega},E,E')[\text{þ}(z)\frac{e^{-\mu z}e^{-\mu' z'}}{|\underline{r} - z\underline{k}|^2}\sigma(\Theta)dz] \qquad [22a]$$

$$= \int dA \int_{\delta\Omega_{det}} d\Omega\ R(\underline{r},\underline{\Omega},E,E') \int_0^D F(z',E')\text{þ}(z)dz/R_2(E,E') \qquad [22b]$$

where z' is the distance travelled in the medium after scattering. If this is substituted into equation 20, and it is observed that for very small flaws, $B_{ref}(E) \sim B_{samp}(E)$ $\sim B_{dif}(E)$

$$D(E) \approx \int_0^{E'} dE' B_{dif}(E') \int_{\delta\Omega} d\Omega\, R(\underline{r},\underline{\Omega},E',E) \int_0^D F(z,E')\delta\text{þ}(z)dz\ /R_2(E,E') \qquad [23]$$

where

$$\delta\text{þ} \approx \text{þ}_{ref} - \text{þ}_{samp}$$

If the multiple scattering factor is known, it is possible to obtain the total differential spectrum from the single scattered spectrum. Likewise, it is possible to calculate the single scattered component from the total spectrum.

The multiple scattering factor can be conveniently calculated using the Monte Carlo methods. This is a statistical means of solving complicated equations by simulating the transport process on a computer. The processes involved in particle transport such as scatter or absorption are described in terms of probability distributions. A particle is allowed to pass through the sample undergoing interactions whose outcomes are determined by the probability distribution. If many particles undertake such random walks, the law of large numbers postulates that the outcome corresponding to this large number of particles will approach an average outcome corresponding to an infinite number of particles. A more detailed discussion of the Monte Carlo code is given in Appendix A.

A more deterministic approach is to look at the time independent integral equation for radiation transport [24,25]:

$$\phi(\underline{r},\underline{\Omega},E) = \int_0^\infty ds' \exp[-\int_0^{s'} \mu(\underline{r}-s''\underline{\Omega},E)ds''] \, q(\underline{r}-s'\underline{\Omega},\underline{\Omega},E) \qquad [24a]$$

where

$$q(\underline{r},\underline{\Omega},E) = \int_0^{E_0} dE' \int_{4\pi} d\Omega' \, F(\underline{r};\underline{\Omega}',E'\rightarrow\underline{\Omega},E)\phi(\underline{r},\underline{\Omega}',E') + S(\underline{r},\underline{\Omega},E) \qquad [24b]$$

$\underline{r}$ = the spatial location of the photon density. The z axis lies along the primary beam path in the cylindrical test object in the direction of the beam, the y axis lies along the axis of the cylinder, the origin is at the beam point of incidence, and the center of the face of the detector lies along the plane y=0.

$\underline{\Omega}$ = the direction of the photon angular density

E = the energy of the photon density

$\mu(\underline{r},E)$ = the attenuation coefficient

$\phi(\underline{r},\underline{\Omega},E)$ = the angular flux density

$F(\underline{r};\underline{\Omega},E'\rightarrow\underline{\Omega},E)$ = the Compton scattering kernel

$S(\underline{r},\underline{\Omega},E)$ = the photon source function, which is 0 everywhere except at the point of incidence of the irradiating beam in the direction of the beam, $\underline{k}$.

If $q(\underline{r},\underline{\Omega},E)$ is substituted into equation 24b , the integral transport equation in operator form becomes

$$\phi = k \cdot [\phi] + S^1 \qquad [25]$$

Again, ϕ can be expressed as an infinite sum of terms

$$\phi(\underline{r},\underline{\Omega},E) = \sum_{n=o}^{\infty} \phi^{(n)}(\underline{r},\underline{\Omega},E) \qquad [26]$$

where $\phi^{(n)}$ represents the contribution to ϕ due to photons suffering n collisions. If this series is substituted into the integral transport equation, the Neumann series results:

$$\phi = \sum_{n=o}^{\infty} k^{(n)} \phi^{(n)} + S^1 \qquad [27a]$$

where

$$S^1 = \phi^{(0)}(\underline{r},\underline{\Omega},E)$$

$$= \int_0^{\infty} ds'\exp[-\int_0^{s'} \mu(\underline{r}-s''\underline{\Omega},E)ds'']S(\underline{r}-s'\underline{\Omega},\underline{\Omega},E) \qquad [27b]$$

$$\phi^{(n+1)}(\underline{r},\underline{\Omega},E) = k\phi^{(n)}$$

$$= \int_0^{\infty} ds'\int_0^{E} dE'\int_{4\pi}d\Omega'\exp[-\int_0^{s'} \mu(\underline{r}-s''\underline{\Omega},E)ds'']\ F(\underline{r}-s'\underline{\Omega};\underline{\Omega}',E'\rightarrow\underline{\Omega},E) \qquad [27c]$$

$$* \ \phi^{(n)}(\underline{r}-s'\underline{\Omega},\underline{\Omega}',E')$$

$$n = 0,1,2,\ldots,\infty$$

To calculate the nth order scattering component it is necessary to know all the lower scattering components since the source for n-scattered particles is n-1 scattered particles. Ideally, the solution can be carried out successively to any order of scattering though it becomes impractical to carry out this integral indefinitely. However, it is possible to calculate some of the lower order scattering components. Since these lower components are more significant than higher order terms, it is possible to approximate the solution.

The zeroth order flux is nonexistent everywhere except in the incident beam, by definition. It does not contribute directly to the flux at the detector, however, it does contribute to $\phi^{(1)}(\underline{r},\underline{\Omega},E)$ as

$$\phi^{(1)}(\underline{r},\underline{\Omega},E) = \frac{I_o\, Z\, A_0\, Z_n\, N_o}{M} \int_0^D dz\,\text{þ}(z)\, e^{-\mu z} e^{-|\underline{r}-z\underline{k}|} \sigma(\Theta)\; d\Omega \quad [28]$$

This is simply the single scattered spectrum determined before and is valid at any point within the medium. If the particle escapes the medium then $|\underline{r} - z\,\underline{k}|$ is replaced by z', where z' is the distance between the point of scattering and the point where the particle exits the medium and $z\underline{k}$ is the vector along the z-axis in the direction of the incident beam from the point of incidence to the point of first scattering.

The second order flux is found by substituting $\phi^{(1)}$ into the recursive relationship (equation 27c)

$$\phi^{(2)}(\underline{r},\underline{\Omega}_1,E) = \int_{L_1(\underline{r},\Omega)}^{L_2(\underline{r},\Omega)} ds_2 \int_{E}^{E_o} dE'' \int_{\delta\Omega} d\Omega'' \; e^{-\mu(E)|\underline{r}-s\underline{\Omega}|} F(\underline{r}-s_2\underline{\Omega}_2;\Omega_1,E_1 \rightarrow \underline{\Omega}_2,E_2)$$

$$\times\ \phi(\underline{r}-s_2\underline{\Omega}_2;\underline{\Omega}_1,E) \qquad [29]$$

The integration procedure is shown in Figure 16. The symbols Θ_n, ϕ_n, $\underline{\Omega}_n$, s_n, and $\underline{r}$ are used to identify the nth polar and azimuthal scattering angles, direction of the photon after the nth scattering interaction, distance traveled in the medium between the n-1 and nth scattering interaction, and spatial location where the photon enters the detector, respectively. If a ray with direction $\underline{\Omega}_2$ passing through point $\underline{r}$ on the face of the detector is traced back through the sample, the chord determined by its intersection with the sample volume constitutes the path of integration, $s_2 \epsilon (L_1(\underline{r},\underline{\Omega}_2), L_2(\underline{r},\underline{\Omega}_2))$. The once-collided angular flux along this path, $\phi^{(1)}(\underline{r}',\underline{\Omega}_1,E)$, can be calculated from equation 28. Because of the strict angle-energy relation, not all angles can contribute to $\phi^{(1)}(\underline{r},\underline{\Omega}_1,E)$. The condition

$$\cos\Theta_1 + \cos\Theta_2 = 2 - 511(\text{keV}) \left(\frac{1}{E} - \frac{1}{E_o}\right) \qquad [30]$$

limits the possible scattering angles, Θ_1 and Θ_2. These scattering angles are also constrained geometrically. For a photon to contribute to ϕ_2 $(\underline{r},\underline{\Omega}_2,E)$ it must collide along the illuminated chord with angle Θ_1, and then once again

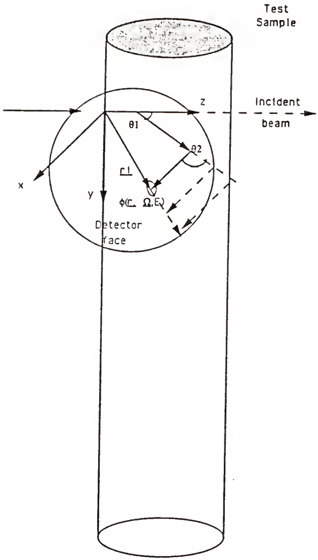

Figure 16. Geometry for twice scattered spectrum.

along its scattered path with angle Θ_2. The calculation of the detector response is performed by letting s_1 vary along the illuminated chord, determining the range of Θ_1, from equation 30, calculating Θ_2 and letting the first azimuthal angle, ϕ_1, vary from zero to 2π. For a given s_1, Θ_1, Θ_2, and ϕ_1 the scheme is to let s_2 vary along direction $\underline{\Omega}_1$ and calculating the range of the second azimuthal angle, ϕ_2, subtended by the detector.

It becomes intractable to calculate higher order spectra. In calculating the twice scattered spectrum it was necessary to let s_1, Θ_1, ϕ_1, s_2, and ϕ_2 vary and additional variables will be required for higher order spectra. The calculation becomes prohibitively time-consuming to calculate the third order spectra.

Figure 17 shows a comparison of the single scattered spectrum calculated using both the Monte Carlo technique and using discrete elements. This calculation was made for a 2.5 cm aluminum test piece with a centrally located .25 cm hole and a 4.43 cm diameter detector located at $(x,y,z) = (1.8,0,1.25)$ and with direction cosines, $(\alpha_D, \beta_D, c_D) = (-1.,0,0)$. Both spectra were normalized so that their maxima were equal. The two calculations agree well over the entire energy range.

The once and twice-scattered spectra for the same test configuration are shown in Figures 18 and 19. The data for Figure 18 was generated with the Monte Carlo technique.

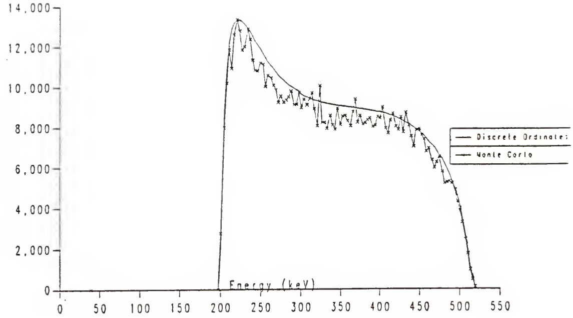

Figure 17. Comparison of Monte Carlo and discrete elements calculation of single scattered spectrum for a centrally located 0.25 cm hole.

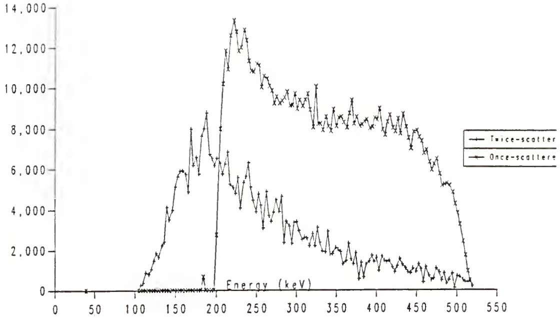

Figure 18. Monte Carlo calculation of once and twice scattered spectrum incident on detector.

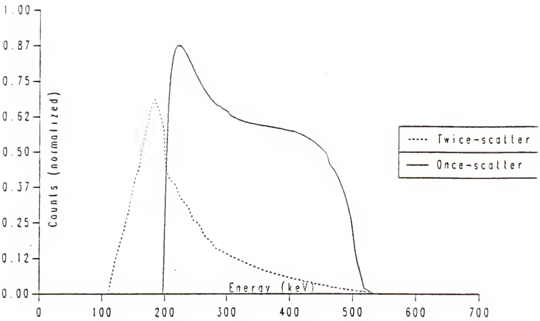

Figure 19. Discrete elements calculation of once and twice scattered spectra incident on the detector.

Notice that in this case the twice-scattered spectrum shows more statistical variance than the once-scattered spectrum. The data for Figure 19 was determined by the discrete elements method. The twice-scattered spectrum is smoother for this calculation.

As discussed previously, when the flaw lies between the detector and the illuminated chord, the differential spectrum is negative. The calculated spectrum (before correcting for the detector response) is shown in Figure 20. Here the differential spectra resembles the once-scattered spectrum only the scattered energy range has expanded. In addition to this slight spread in the differential spectrum, the intensity is much smaller. The maximum intensity for a flaw off the illuminated chord, as calculated by the Monte Carlo method, is three orders of magnitude smaller than the intensity for a flaw located on the illuminated chord. At energies below about 180 keV, multiple scattering in the flaw region contributes significantly and the spectrum may become positive.

When the flaw is located on the opposite side of the illuminated chord, the differential spectrum is positive for all energies (see Figure 21). At higher energies the spectrum is very small but increases rapidly at lower energies where multiple scattering can contribute. The maximum intensity for these flaws is even smaller than for those flaws on the opposite side near the detector. It becomes quite difficult to detect such flaws.

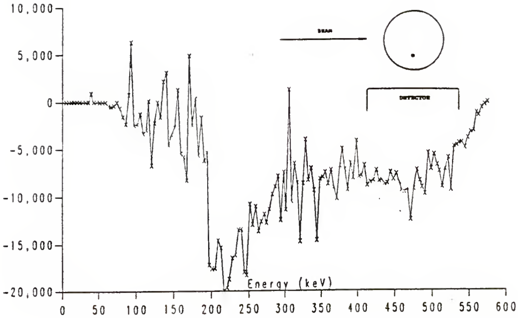

Figure 20. Monte Carlo calculation of differential spectrum from a 0.25 cm hole located at x = 0.626, z=1.25 cm.

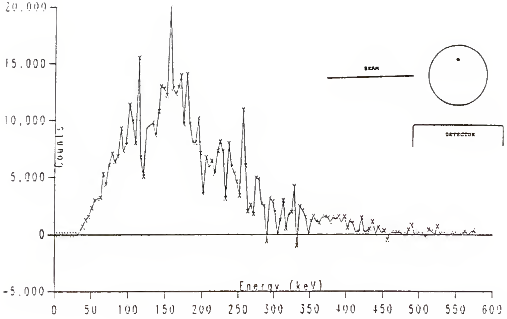

Figure 21. Monte Carlo calculation for a 0.25 cm hole located at x=-.625, z=1.25 cm.

CHAPTER 4
INVERSE TRANSPORT METHODS

Simple Matrix Inversion

We have just discussed the usual problem of calculating the scattered radiation incident on an observer (the detector) for a given source and scattering media characterized by well-known material constants. The case of the once-scattered spectrum is easily calculated using discrete elements and the total spectrum can be calculated by a Monte Carlo calculation. This is the direct problem.

The inverse problem is of interest in non-destructive testing. Here the scattered spectrum and the source are completely defined. The material properties of the scattering medium (such as scattering cross-sections and material densities) are also already known. The objective is to calculate the scattering medium density distribution.

The differential spectrum is obtained from experiment and stored in a multi-channel analyzer. Detector systems are capable of counting gamma-rays, determining their energies, sorting them by energy and storing the number of counts for each energy in an energy bin or channel. This equates to computing an energy distribution, i.e., the number of counts in dE about E. However, as noted previously, it is desirable to know the distribution of counts by scattering angle, not energy, in order to determine the location of the sample. This can be accomplished since there exists a one-to-one correspondence between scattering energy and scattering angle,

$$E = \frac{E_o}{1 + \frac{E_o}{511}(1-\cos\Theta)} \qquad [31]$$

Therefore it is quite possible to manipulate the energy spectrum N(E)dE to obtain the scattering angle distribution, N(Θ)dΘ.

The procedure for mathematically inverting the problem can best be seen by investigating the scattering process. Figure 22 below shows schematically the scattering of radiation from a collimated source by a cylindrical sample placed with its diameter lying along the path of the collimated beam. If it is assumed that photons are permitted to interact only once while passing through the sample (single scattering only) the problem is greatly simplified and is easily visualized. Later corrections are incorporated into the procedure allowing multiple scattering. The illuminated chord is discretized into a number of small pixels and scattering for each pixel is analyzed as though it were a point. Each pixel will have associated with it a spectrum of scattered photons subtended

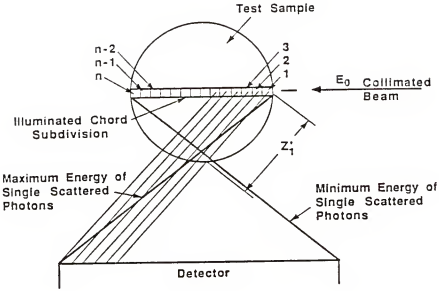
Test Sample
n-2
n-1
n
3
2
1
E_0 Collimated Beam
Illuminated Chord Subdivision
Z_1'
Maximum Energy of Single Scattered Photons
Minimum Energy of Single Scattered Photons
Detector

Figure 22. Pixel representation of illuminated chord used for calculation of the differential spectrum.

by the detector. The detector will thus see a broad spectrum of energies ranging between a minimum arising from pixel n and a maximum arising from pixel 1, closest to the source. Mathematically the total spectrum as is incident on the detector will be:

$$N(E)dE = \int_{0}^{D} dz \; [I_o \; \frac{\delta \rho(z)}{M} \; A_o Z_n \; e^{-\mu z} \; e^{-\mu' z'} \; \sigma(\Theta)]d\Omega \qquad [32]$$

where N(E) = the number of photons striking the detector with energy E in dE (ignoring multiple scattering)

If this equation is discretized according to our pixel representation, then

$$N(E)dE = \sum_{i=1}^{n} w_i \; \frac{I_o N_o Z_n}{M} \; \rho_i e^{-\mu z} \; e^{-\mu' z'} \; \sigma(E_o \rightarrow E)d\Omega \qquad [33]$$

where w_i is a weighting factor appropriate for the selected method of numerical integration and $\sigma(E_o \rightarrow E)$ is the differential cross section for scattering an angle

$$\Theta = \cos^{-1}[1-511 \; (\frac{1}{E} - \frac{1}{E_o})]$$

This equation can also be discretized in the energy variable,

$$N_{i,j} = \sum_{i=1}^{n} w_i (\frac{I_o N_o Z_n}{M}) \; \rho_i e^{-\mu z} \; e^{-\mu' z'} \; \sigma(E_o \rightarrow E_j) \, \delta\Omega \qquad [34]$$

The choice of energies is arbitrary. If n such energy groups are chosen corresponding to n pixels, n equations in n unknowns result. In matrix form this is written, $\underline{N} = \underline{M}\ \underline{b}$ from which the problem can be inverted and the vector of material densities can be at least theoretically calculated, $\underline{b} = \underline{M}^{-1}\underline{N}$.

The problem of inverting the matrix M may be difficult if the energies are not properly chosen. If the energy range is uniformly subdivided into n groups the subsequent matrix will be ill-conditioned. However if the energies are properly chosen the matrix can be constrained to be upper triangular and easily inverted. Figure 23 shows the scheme for selecting such energies. If the discrete energies are chosen to correspond to the maximum scattering energies possible for each pixel, then the matrix must be upper triangular. For example, E_1 is within the range of all pixel scattering spectra. However, E_1 is in the range of all pixel scattering spectra, except for pixel Z_1. Each subsequent energy group has one fewer pixel associated with it until finally only pixel Z_n contributes to energy group E_n.

Method of Least Square Fit

A variant of the matrix method for calculating the density distribution along the illuminated chord is the method of least square fit. As was mentioned above, the

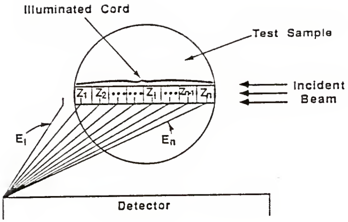

Figure 23. Selection of scattering energies to guarantee an upper triangular scattering matrix.

matrix method has certain numerical problems. The method may require smoothing or a selective choice of energy points to improve the numerical stability. Even so, the random statistical variation of the measured detector response leads to a linear set of equations that is not completely determined.

In the matrix method it was necessary to write out the equations for the forward problem and then inverting the matrix equation. We can calculate a differential spectrum, $\underline{Ds}_i$, for each pixel location, i, by assuming that the pixel behaves as a point centered in a differential volume with cross-sectional area equal to that of the beam and length determined by the number of pixels. In the forward problem, the measured differential spectrum, $\underline{D}$, can be calculated by weighting each pixel differential spectrum, Ds_i, by the perturbation from nominal density at that pixel location. In detail it is described by the matrix equation, $\underline{D} = \underline{M}\ \underline{\rho} + \underline{\epsilon}$, or

$$D = \begin{bmatrix} m_{1,1} \\ m_{2,1} \\ \vdots \\ m_{n,1} \end{bmatrix} \rho_1 + \begin{bmatrix} m_{1,2} \\ m_{2,2} \\ \vdots \\ m_{n,2} \end{bmatrix} \rho_2 + \dots + \begin{bmatrix} m_{1,n} \\ m_{2,n} \\ \vdots \\ m_{n,n} \end{bmatrix} \rho_n + \epsilon \qquad [35]$$

or

$$\underline{D} = \underline{Ds}_1\ \underline{\rho}_1 + \underline{Ds}_2\ \underline{\rho}_2 + \ .\ .\ .\ \ \underline{Ds}_n\ \underline{\rho}_n + \underline{\epsilon} \qquad [36]$$

Now the accumulated spectrum, $\underline{D}$, is a vector that results from experimental measurements and will have an uncertainty vector associated with it, $\underline{\epsilon}$. The pixel differential spectra, $\underline{DS}_i$, ideally will be well defined and have no uncertainty since the geometry of the reference problem and the material properties are well-known. This assumes that the flaw is small that the differential spectra, $\underline{DS}_i$, are not greatly effected by a flaw at any other location. The statistical error, $\underline{\epsilon}$, is unknown so the problem of calculating the weights, ρ_i, is not completely determined. Now, since the weights are calculated from $\underline{D}$, they also will have uncertainty associated with them. The objective of the method of least square fit is to minimize that uncertainty.

Since in our experiments we are only looking for holes or regions where the test sample density goes to zero, the weights, ρ_i, which correspond to density cannot be negative. In fact, if the pixels are chosen finely enough, the weights can take only two values, the nominal density or 0 (either there is a hole or not). There will be places where a hole may only partially intersect with a pixel but if the number of pixels is small compared to the size of the hole, these pixels will contribute little to the overall differential spectrum.

The method proceeds by assuming a density distribution, $\rho(z)$, and comparing the corresponding calculated spectrum with the measured spectrum. But this choice for the density distribution was arbitrary and other possible density distributions can be assumed. The density distribution whose corresponding calculated scattered spectrum most closely agrees with the measured spectrum is accepted as the solution.

First assume that the hole consists of only one pixel, i,

$$\delta \text{þ}_i = \begin{cases} 0 & \text{for} \quad i \neq j \\ \text{þ} & \text{for} \quad i = j \end{cases} \qquad [37]$$

Notice that subtracting the test sample spectrum from the reference spectrum to obtain the differential spectrum yields the seemingly contradictory results that at the hole,

$\delta \text{þ}_i = \text{þ}$. This is because mass exists, or scattering occurs, at the hole location in the reference sample and not in the flawed test piece.

Now the calculated differential spectrum, $\underline{D}^{(1)}$, is compared with the measured differential spectrum, $\underline{D}$. The least square error is used to quantify this comparison. It is defined as

$$\epsilon^{(n)} = \frac{\left(\sum_{i=1}^{n} (r_i - \mu)^2 \right) / n}{\left(\sum_{n=1}^{n} (r_i) \right)^2 / n^2} = \sigma^2 / \mu^2 \qquad [38a]$$

$$\text{where} \quad \mu = \sum_{i=1}^{n} r_i / n \qquad [38b]$$

and $$r_i = \frac{D_i}{D_i^{(n)}} + \frac{D_i^{(n)}}{D_i} \qquad [38c]$$

The error is defined as the variance in the ratio of the pixel differential spectrum to the differential spectrum, normalized by the average of this ratio. Notice that if the measured spectrum goes to zero where the pixel spectrum predicts a nonzero value, the error is infinite and that particular choice of pixel location is disregarded.

If the hole is only as large as one pixel, the problem is solved. However for larger holes, the procedure continues. Now the hole is allowed to "grow" to surrounding pixels. First a neighboring pixel is assumed to contribute to the hole and the error is calculated, then another neighboring pixel is added. The hole may also be allowed to "shrink" or migrate by removing edge pixels. The process continues until the error begins to increase. The accepted hole size corresponds to a minimum least square error.

Two holes located along the illuminated chord can be assumed by first determining the minimum least square error for two disconnected pixels. These pixels are then allowed to "grow" in the same manner as for the single hole. It may be possible that the two hole grow together into one hole, in which case it is assumed that there is, in fact, only one hole.

Above we have assumed a number of holes in the test sample to simplify the problem. One may wish not to assume any number of holes and test all combination of vacant or nonvacant pixels. For example, for 3 pixel locations there are 8 combinations of vacant/non-vacant pixels. If we let 1 correspond to a vacant pixel (hole) and 0 to nonvacant pixels, the set of combinations is represented in set notation by:

$$\{(1,0,0),(0,1,0),(0,0,1),(1,1,0),$$
$$(1,0,1),(0,1,1),(1,1,1),(0,0,0)\}$$

More generally for an arbitrary number of pixels, n, there will be 2^n combinations of vacant and non vacant pixels. As an example, if 20 pixels are chosen along the illuminated chord, there would be $1\text{x}10^6$ combinations: a prohibitively large number of combinations to check out. If it can be safely assumed that only 1 or 2 small holes lie along the illuminated chord the problem becomes more tractable.

The method of least squares can numerically tolerate the statistical variation in the measured spectra. Since the calculation proceeds by fitting spectra from known density distributions to measured spectra and determining the statistical deviation it is not necessary to smooth the raw data before analysis.

Figure 24 shows the density distributions along the incident beam path calculated for three hole sizes located at the center of the test sample. The differential spectra, $\underline{D}$, that were used as input (equation 35) were not actual measured data but rather were calculated for the three hole sizes. These spectra were calculated

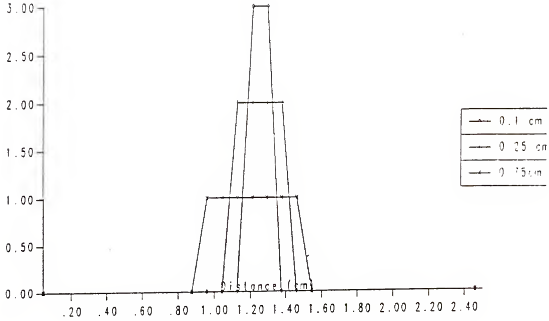

Figure 24. Calculation of density profile along illuminated chord by least square method using exactly calculated differential spectra for three holes sizes 0.1, 0.25, and 0.75 cm.

using discrete elements methods so there is no statistical variation associated with the input. The results reliably predict the hole size and location. Figure 25 used actual measured spectra as input with inherent statistical uncertainties associated with them. Hole location again is well determined, but it was not possible to calculate hole size with the same degree of reliability.

There are other methods for unfolding the Fredholm equation, $\underline{N} = \underline{R}\ \underline{S} + \underline{\epsilon}$, that do not require any assumptions about the density distribution [26]. The procedure is to find an unbiased vector estimate $\underline{S}'$ for the vector $\underline{S}$. An unbiased estimation implies that the expectation of $\underline{S}'$ is the true vector $\underline{S}$, or written symbolically, $E[\underline{S}'] = \underline{S}$. A linear vector function of the form $\underline{S}' = \underline{U}\ \underline{N}$ giving $\underline{U}\ E[\underline{N}] = \underline{S}$. It is assumed that the error array is randomly distributed so that $E[\underline{\epsilon}] = 0$. It follows that $E[\underline{N}] = \underline{R}\ E[\underline{S}]$ and $\underline{U}\ \underline{R} = \underline{I}$.

The variance of the estimator is minimized subject to the constraint above for an unbiased estimator by the method of Lagrange where the Lagrangian function to be minimized is

$$\underline{L} = \underline{U}^T\underline{V}\ \underline{U} + (\underline{U}^T\underline{R} - \underline{I})\ \underline{p} \qquad [39]$$

where $\underline{p}$ is a vector of lagrange multipliers. The best linear estimator can then be calculated from:

$$\underline{U} = (\underline{R}^T\underline{V}\quad \underline{R})\quad \underline{R}\ \underline{V} \qquad [40]$$

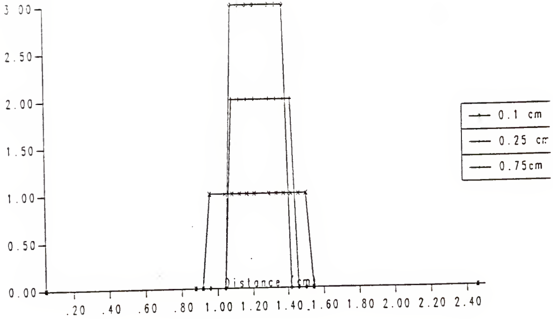

Figure 25. Calculation of density profile along illuminated chord by least square method using measured differential spectra.

where $\underline{V}$ is the variance matrix of the vector $\underline{S}$

$$\underline{V} = E[\underline{\epsilon}\ \underline{\epsilon}^{T}] = E[(\underline{S}-E[\underline{S}])(\underline{S}-E[\underline{S}])] \qquad [41]$$

= {0 when i#j and σ_{ij} otherwise}.

CHAPTER 5
DATA CORRECTION METHODS

Compton Energy Broadening

An assumption made early on was that in Compton scattering there is a one-to-one correspondence between the polar scattering angle and the energy of the scattered photon, $E = Eo/(1. + Eo/511*(1-\cos(\Theta))$. This is strictly true when the target electron behaves as a free particle at rest or such that its binding energy can be neglected and when the energy imparted to an electron is not so great that relativistic effects are important. When relativistic effects become important, the energy of the scattered photon is not limited to a discrete energy E' as is determined by the angle/energy relationship above. Instead, photons will acquire energies from a narrow distribution about E'. The distribution becomes less broad as relativistic effects become less important. In the limit when relativistic effects can be neglected, the distribution is infinitesimally narrow and the energy is fully determined by the angle/energy relationship.

An approximate form for the differential Compton cross-section is derived by Ribberfors [27]. It utilizes the impulse approximation, assuming the energy transferred to the electron is large in comparison to its binding energy. But it does take into account relativistic effects due to transfer of large amounts of energy from the photon to the electron.

The resulting approximate equation for the differential cross-section is written

$$\frac{d^2\sigma}{d\Omega' dE'} = \frac{m_0 r^2}{2|p-p'|} \quad \frac{E'}{E} \; [\frac{E}{E'} + \frac{E'}{E} - \sin^2\Theta] \; J(p_z) \quad [42a]$$

where (p,E) and (p',E') are the momenta and energies of the photon before and after collision, respectively, and

$$|p-p'| = \frac{1}{c} [E^2 + E'^2 - 2EE'\cos\Theta]^{1/2} \qquad [42b]$$

$$p_z = [EE'(1-\cos\Theta) - m_o(E-E')]/|p-p'| \qquad [42c]$$

= the projection of the electron momentum on the scattering vector

$J(p_z) = 2\pi \int_{|p_z|}^{i} dp \; p \; þ(p)$ = the Compton profile

$þ(p)$ = the momentum distribution of the initial state

m_o = 511 keV = the election rest mass

r_o^2 = 7.95 x $10^{-30} m^2$ = the square of the classical electron radius

The Compton profile, $J(p_z)$, has been experimentally determined by several sources [28, 29, 30]. Tabulated values for $J(p_z)$ for aluminum were used to calculate the differential cross-section for aluminum at source energies of 59.54 and 661.5 keV and scattering angles of 90° (see Figure 26). Notice that in correcting for relativistic effects the cross-section is altered by a spread about the non-relativistic value. This spread, characterized by the

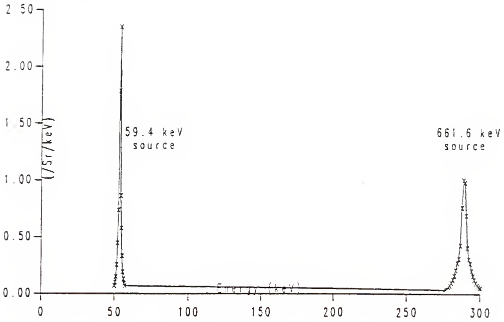

Figure 26. Differential cross-section showing Compton broadening at a scattering angle of 90°.

full width at half maximum, Γ_{comp}, increases with the incident photon energy. It also increases with polar scattering angle as more energy is transferred to the target electron. It also becomes more important as the atomic number of the scattering material increases. These effects are shown in Figures 27, 28, and 29.

Statistics

The method of DGSS has been verified by experimentally obtained differential spectra. When spectra from flawed test samples are compared with reference spectra from unflawed samples, the appearance of a differential spectra is an indication of the flaw. Because of the statistical nature of radiation and the finite counting time of the experiment, the spectra will show a statistical scatter about an average distribution. This statistical spread can be characterized by the variance, σ_i. If Nr_i is the number of counts in the reference spectrum and Ns_i the number of counts in the scattered spectrum, the variance in the differential spectrum is found from [31]:

$$\sigma_i = \quad (Nr_i + Ns_i)^{1/2} \qquad [43]$$

$$(Nr_i^{(0)} + Ns_i^{(0)} + Nr_i^{(b)} + Ns_i^{(b)})^{1/2}$$

where the superscript $^{(0)}$ refers to that component of the total reference spectrum that contributes to the differential spectrum and $Nr_i^{(b)}$ and $Ns_i^{(b)}$ refer to the

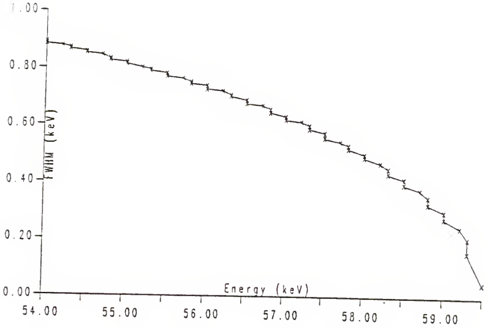

Figure 27. Calculated Compton broadening FWHM for a photon with energy 59.4 keV scattering in aluminum.

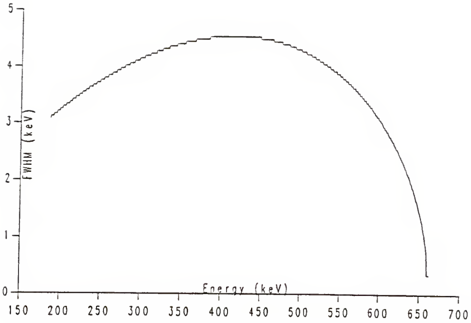

Figure 28. Calculated Compton broadening FWHM for a photon with energy 661.6 keV scattering in aluminum.

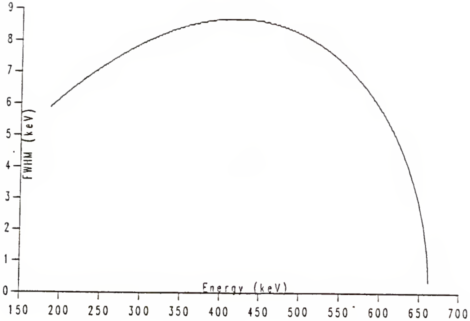

Figure 29. Calculated Compton broadening FWHM for a photon with energy 661.i6 keV scattering in iron.

balance or background of the reference and sample spectra, respectively.

This has several implications. Notice that the sum, $Nr_i + Ns_i$, and not the difference, $Nr_i - Ns_i$, appears in this equation. This means that all events, even those not contributing to the differential spectrum, will contribute to the variance. In reducing the variance it is therefore necessary to try to eliminate all events not contributing to the differential spectrum. Significant variance reduction can be obtained by properly shielding the source from the detector or by reducing back-scatter from objects surrounding the experiment.

The statistics of an experiment can also be improved by increasing its counting time. If both the reference and sample are counted for the same length of time, then

$$\sigma_i = t^{1/2} \quad (Cr_i + Cs_i)^{1/2} \qquad [44]$$

where Cr_i and Cs_i are the count rates for the reference and sample spectra respectively. The variance then increases in time without bound. If it is further assumed that for small flaws Cr_i and Cs_i are so close that $Cr_i + Cs_i = 2\,Cr_i$, then the variance as a fraction of the differential spectra is

$$\frac{\sigma_i}{(Nr_i - Ns_i)} = t^{-1/2} \frac{[Cr_i^{(0)} + Cs_i^{(0)} + Cr_i^{(b)} + Cs_i^{(b)}]^{1/2}}{Cr_i^{(0)} - Cs_i^{(0)}} \qquad [45a]$$

$$\approx \quad (2/t)^{1/2} \frac{(1 + f)^{1/2}}{S_o^{1/2} \quad (Xr_i^{(0)} - Xs_i^{(0)})^{1/2}} \qquad [45b]$$

where f is the ratio of detected events not contributing to the differential spectra to those that do, $f = Cr_i^{(b)} / Cr_i^{(0)}$, S_0 is the source strength, Xr_i and Xs_i are the fraction of source photons contributing to the differential spectrum, $Xr_i = Cr_i / S_0$, and $Xs_i = Cs_i / S_0$. This shows that even though the variance increases in time without bounds, the relative spread in scatter about the expected value decreases in time. Spectra become clearer and show more detail with longer accumulation times. However, this fractional variance decreases only at the rate of the inverse of the square root of time. For example, the fractional variance for an experiment could be cut in half by increasing the accumulation time four-fold. Since the accumulation time required to detect fine flaws present in a test specimen may be quite large, it may not be practical in all cases to achieve any improvement by varying this variable. Figure 30 shows a time-elapsed development of the DGS. The accumulation time of the test spectrum has been doubled between successive frames. The reference sample was collected in 64,000 seconds. For this case, collection times less than 1000 seconds provide statistics that are adequate for flaw detection. A useful application may require a reference spectrum collected for more than 64,000

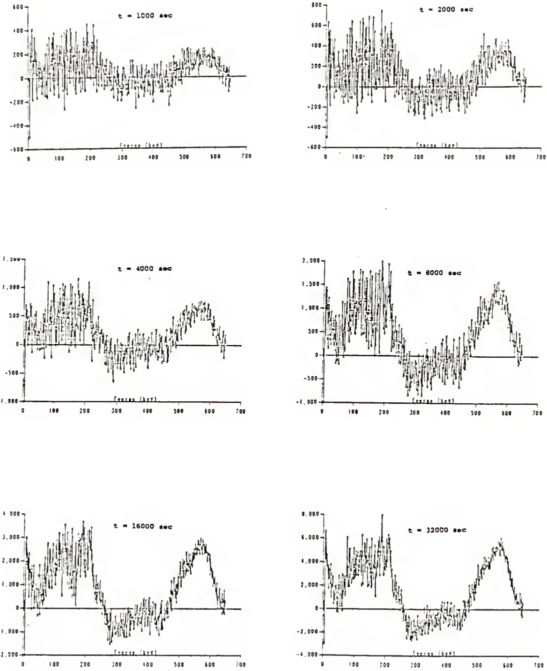

Figure 30. Time elapsed view of differential spectrum.

seconds but the flawed test spectra may need only collection times on the order of several minutes.

It is also observed that the fractional variance can be reduced by going to higher source strengths. This is not strictly true since increasing the source strength may increase the factor f; more source photons will be transmitted through the shield and interact in the detector without interacting in the test object. To improve the statistics, the beam strength should increase without increasing the number of extraneous photons to the detector excessively.

It is also of interest to determine just how the fractional variance may change with the flaw size. The fractional variance can be written in terms of the reference and test sample spectra:

$$\frac{\sigma_i}{(Nr_i - Ns_i)} = \frac{(Nr_i + Ns_i)^{1/2}}{(Nr_i - Ns_i)} \qquad [46]$$

If it is assumed that only once scattered photons contribute to the two spectra and that the flaw is located along the illuminated chord, then equations 12, 13, and 14 can be substituted into equation to obtain the approximate solution

$$\frac{\sigma_i}{Nr_i - Ns_i} = \frac{1}{C} \quad \frac{[2\int_0^{L_D} e^{-(L+L')}dL - e^{-(L(k)+L(k)')}\delta L_k]^{1/2}}{e^{-(L(k)+L(k)')}\ \delta L_k} \qquad [47a]$$

where $L = \mu z$, $L' = \mu' z'$, $\delta L_k = \mu \delta z_k$, $L_D = \mu D$, D = length of the illuminated chord, and for a cylinder whose diameter coincides with the illuminated chord,

$$Z' = -(Z - \frac{D}{2}) \cos\Theta \pm (z - \frac{D}{2})^2 \cos^2\Theta - Z(Z-D) \qquad [47b]$$

As the hole size goes to zero the fractional variance becomes infinitely large:

$$\frac{\sigma_i}{Nr_i - Ns_i} \sim \frac{1}{\delta L_k} \qquad [48]$$

It becomes more and more impractical to detect progressively smaller flaws because the variance may overwhelm the differential spectrum.

The length of the illuminated chord and the position of the flaw will also effect the fractional variance. As the sample diameter increases so does the value of the integral in equation 47. Also, as the flaw is located deeper in the material, L_k increases and so does the fractional variance.

If the spectra from two identical samples are compared, the differential spectra that results is characterized by an average of zero superimposed by random statistical variation. It may be difficult to determine just by looking whether there is any statistical significance to data points. An analytical means of making this decision must be used. As would be expected it utilizes the statistical variation discussed above.

The variance, σ_i, calculated in equation 42 can be used to determine the probability that the difference, D_i, is statistically significant or not. If it is assumed that the difference should be zero, the probability that the difference is between $-D_i$ and $+D_i$ for a normal distribution is given by

$$p_i = \int_{-D_i}^{D_i} 1/\sigma_i \ (2/\pi)^{1/2} \ \exp(-x^2 /2\sigma_i^2) \quad dx \qquad [49]$$

This is also the probability that the difference, D_i, deviates from just statistical scatter superimposed on a zero differential spectrum. If this probability is sufficiently large, then the difference at channel i is accepted as being non-zero. Unless the window of acceptable probabilities is set sufficiently high, the number of counts in one or two isolated channels may be sufficiently high to signify the existence of a flaw. However, if a flaw exists, it will effect the number of counts in a series of connected channels. A better method then would be to look at groups of channels. If the probability that the differential spectrum is non-zero at channel i is p_i and the probability that the difference obtained from adjacent channel i+1 is p_{i+1}, then the probability that both channels are non-zero is $p_i \cdot p_{i+1}$. This can be extended to k adjacent channels.

$$P_k = \prod_{i=1}^{k} P_i \qquad [50]$$

A small pixel of size dz would have a broad energy range effecting k energy channels. The procedure for determining whether the count at any particular channel is non-zero is to determine p_k for all sets of consecutive channels containing channel i. If any one set has a sufficiently high probability, then i is assumed to be non-zero.

Table 1 shows how the probability that the differential spectrum of Figure 30 changes with time. As indicated, the strong upper energy curve is statistically significant for all times greater than 1000 seconds. The lower negative portion of the differential spectrum in the range 250 keV to 480 keV does not become significant until about 16000 seconds where 30 channels are affected. These statistics improve even more as the experiment is carried out indefinitely.

Table 1. Probability, P_n , that n channels of the DGS display statistically significant deviations for a reference sample collected in 64,000 sec.

Test Sample Accumulation Time (sec)	Energy Range			
	290-420 keV			290-600 keV
	P_{50}	P_{30}	P_{20}	P_{50} , P_{30} , P_{20}
2000	0	0	0	1
4000	0	0	0	1
8000	0	0	0	1
16000	0	.32	.52	1
32000	.072	.25	.55	1
64000	.36	.695	.808	1

CHAPTER 6
EXPERIMENTATION AND RESULTS

Gamma-ray Source

A convenient feature of the DGSS technique is that portable gamma sources can be used providing a means by which components can be tested in service. There are a wide variety of gamma sources to choose from. Selection is based on radiation half-life, the number of different gamma-rays emitted, the energy of the gamma-ray and the cost. The ideal source should be inexpensive, have a long half-life for practical use and emit gamma-rays of only one or two energies so that analysis is simplified. The choice of energy may be based on scattering characteristics.

As described in the previous chapter, an underlying assumption in early developments was that Compton scattering is the major contribution to scattering. There are, however, other modes of scattering possible for photons, i.e. pair production, photoelectric absorption, and Rayleigh scattering. We also neglected the scattering of source photons in air. When source photons are chosen with appropriate energies we are justified in making these assumptions. This is not to say that these scattering modes must be avoided for differential spectra. In fact, pair production might be appropriately incorporated into the DGSS technique. But for this study it was avoided.

Pair production involves the interaction of a photon in the Coulomb field closely surrounding a nucleus. The photon disappears and is replaced by an electron and a positron. From energy considerations we can generally assume that pair production contributes nothing to the differential spectra. This is strictly true if the energy of the source photon is less than the threshold energy corresponding to the rest mass of 2 electrons, 1.022 MeV. More practically, pair production is not significant until the energy of the source photon is almost 2 MeV. If pair production were to be strictly avoided, it might be necessary to rule out such isotopes as Co-60 and Na-22.

Photoelectric absorption and Rayleigh scattering become important at lower energies. The energy for which the photoelectric effect tends to dominate varies with the scattering media (it increases with the atomic number) but it is approximately 0.1 MeV and 0.5 MeV for water and lead respectively.

If the energy of the source photon is selected from an intermediate range between 0.10 MeV and 2.0 MeV, Compton scattering will dominate. Photons become more penetrating as their energies increase favoring high source energies. Conversely, the detector efficiency tends to decrease with increasing energy so the preference which favors lower energy sources. Selected for the experiments conducted in this paper was a 0.6 Ci Cs-137 source which emits a 661.6 keV photon. Sources much larger could be used to improve the statistics of a scattering experiment. However, larger sources were not available at the time of the experiment. Acquisition of a larger source could have delayed the research by many months because of the problems associated with licensing, shipping, and shielding. The 0.6 Ci Cs-137 source was adequate for the sensitivity experiment of this report. The small encapsulated source is housed in a large lead cask 19.4 cm in diameter. This provides nearly 7 cm of shielding for the source.

In the side of the lead cask a small 0.25 cm diameter hole is drilled radially outward from the central cavity. This hole serves as the primary collimator for the source beam. In addition, a 3.7 cm thick block of lead is placed between the test object and the exit point of the beam on the cask surface. This serves as a secondary collimator. If the block is placed 5.5 cm from the cask the beam divergence is less than 2°. A laser beam is used to align the narrow source beam and the object. The cask can also be opened and the source inside can be adjusted using a mirror and tongs to provide the maximum beam strength. A beam strength of 2.7×10^6 photons/cm^2 -sec is possible when the object is placed a distance of 25 cm from the cask surface. In a 0.254 cm beam this is equivalent to 1.3×10^5 photon's/sec incident on the test piece.

Test Samples

Tests have been conducted on a number of test specimens to assess the sensitivity of the system to various experimental conditions. Flaw position and flaw size are two parameters that have been varied in this sensitivity study.

A cylindrical aluminum sample 10 cm high and 2.5 cm in diameter was used as both a reference and test sample. A simulated flaw was introduced in one end of the sample in the form of a 3 cm long cylindrical hole drilled parallel to the sample axis. Four hole sizes were investigated: 0.75 cm, 0.50 cm, 0.25 cm and 0.10 cm. There were two samples constructed for each hole size, one with a centrally located hole and another with the hole offset 0.625 cm from the sample center. These two samples allowed testing of three hole locations along the illuminated chord (see Figure 31).

The sample with the offset hole could also be used to assess the abilities of the system to detect holes that do not lay on the illuminated chord. The sample can be rotated 360° to examine a variety of hole locations. Angles 90° and 270° in particular were examined to show how the differential spectrum changes as the flaw is reflected across the illuminated chord.

Another test piece that was examined had three holes implanted to test the ability to resolve more than one hole (see Figure 32). The sample was a 3.3 cm diameter aluminum cylinder that was 10 cm long. The three 3 mm diameter holes implanted along the diameter were 3 cm deep and spaced 0.6 cm apart.

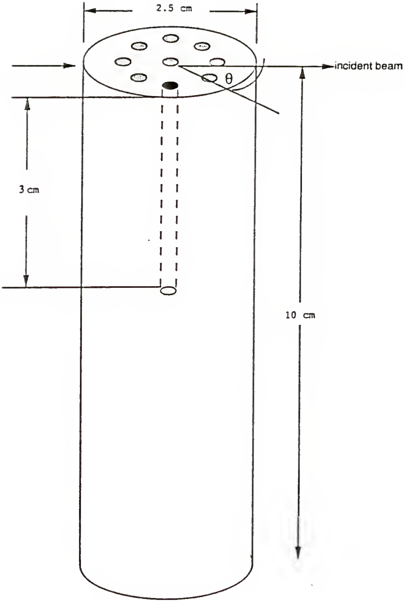

Figure 31. Test specimen for sensitivity study of hole location.

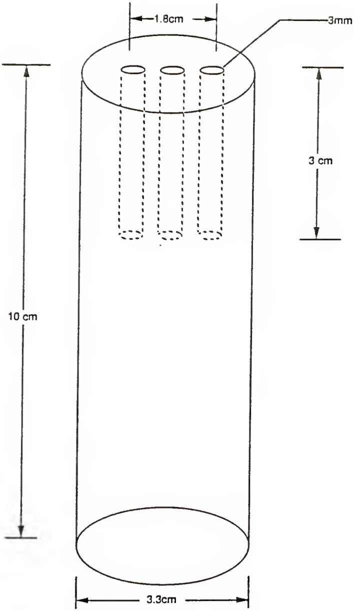

Figure 32. Test specimen for detection of three holes.

The DGSS technique may have useful application in the study of piping. In routine service, piping can acquire a variety of defects. The testing technique should be able to detect these defects including pitting, internal deposits, gouging, cracking and wall thinning.

Three samples have been fabricated to test the inspection capabilities for these flaws. The first sample consists of a 1 inch inner diameter pipe. The pipe is 4" long and consists of two 2" regions. The pipe in the lower 2" section is 0.25" thick while the upper half is 0.125" thick. This sample simulates thinning of the outer wall (see Figure 33).

The second sample is a 2" diameter aluminum cylinder with a tapered central hole (see Figure 34). The hole diameter changes linearly along the axis from approximately 2" to 0" diameter. This sample is capable of simulating thinning of the inside diameter of an aluminum pipe. Pipe thicknesses from 1/32 " to 1" can be modeled.

The final sample is a 1.5" diameter pipe with several simulated flaws implanted on the inner wall. This sample is capable of modeling 1/4" and 1/2" diameter pits, a 1/4" gouge, and a narrow 0.046" crack. The sample is diagrammed in Figure 35.

Detector

The measurement of the scattered spectrum is crucial to all subsequent computational analysis. For meaningful

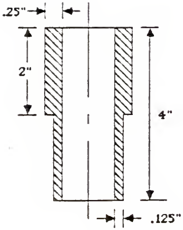

Figure 33. Test specimen for outer wall thinning.

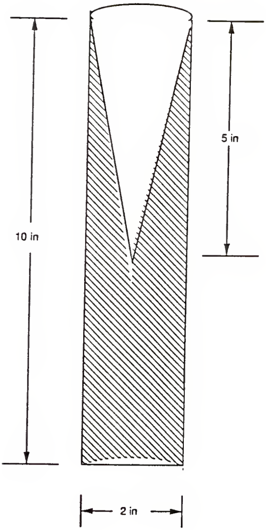

Figure 34. Test specimen for inner wall thinning.

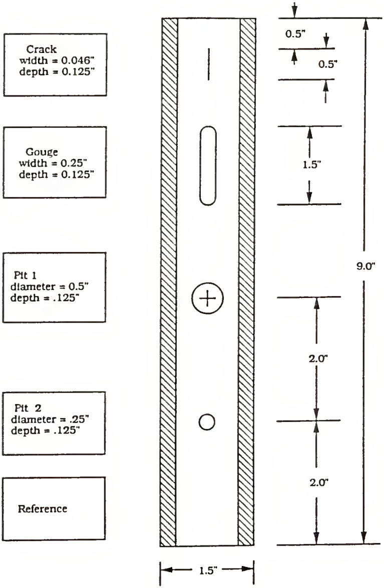

Figure 35. Test specimen for pipe with four implanted service flaws

results, the experimental data should closely resemble the true scattered spectrum incident on the detector. Therefore at the heart of the DGS technique lies the detector and its associated electronics.

The detector is an EG&G Ortec GEM series high purity Germanium (HPGe) detector. It is a p-type coaxial detector with a 0.7 mm lithium diffused outer contact and a thin ion implant inner contact that is less than 3 microns thick. The germanium crystal is 4.57 cm in diameter and 5.26 cm in length. It is protected by a 1.27 mm aluminum cap with a spacing of 0.3 cm between end cap and crystal.

The HPGe detector offers excellent resolution for photons in the range of 50 keV to almost 10 MeV. Ideally the spectrum of photon energies from a radioactive source that emits a monoenergetic photon will generate a dirac delta- function response centered at the photon energy. Because of random noise in the detection system, the spectrum near E_0 will be broadened into a shape that closely resembles a Gaussian curve. The full width at half maximum, Γ, for a photo-peak of energy 1.33 MeV is only 1.71 keV. At 122 keV, Γ, is as small as 762 eV. The resolution was measured for a number of photon energies by analysis of the spectrum of gamma rays emitted from a Eu-152 calibration source. Eu-152 provides gamma rays with energies ranging from 121 to 1457 keV. A polynomial was fit to these data in a least-square sense to be used for data correction.

The system noise arises from two components: the detector, Γ_d, and the associated electronics, Γ_e. The system noise is obtained by adding the two in quadrature: $\Gamma_{sys}^2 = \Gamma_d^2 + \Gamma_e^2$. The detector resolution is given approximately by the theoretical value $D = 2.35 \sqrt{\epsilon FE}$ where the Fano factor, F, is 0.1, the energy, ϵ, required to create a hole pair is 2.97 eV, and E is the photon energy in eV.

Compton broadening is another contribution to the overall resolution and was discussed in a previous section. It too is added in quadrature to the system resolution to determine the total resolution, i.e., $\Gamma_{tot} = \Gamma_d^2 + \Gamma_e^2 + \Gamma_{comp}^2$.

The signal from the preamplifier is then directed to an ORTEC 572 spectroscopy amplifier for further processing and shaping. The amplifier has an input impedance of approximately 500 Ω and accepts either positive or negative input pulses with rise times < 650 μs. There are 6 integrate and differentiate time constants that may be selected by the user. The proper time constant is determined by the system noise. The electronics noise can be resolved into 3 primary components: series noise, parallel noise, and 1/f noise. The total noise can be estimated from these components which are functions of either the shaping time, τ, or the frequency, f, by:

$$N \approx \frac{C_i}{\sqrt{\tau}} + C_2 \sqrt{\tau} + \frac{1}{f} \qquad [51]$$

From this dependence of noise on shaping time it is obvious that there is an optimum for which the noise is a minimum. A time constant of 6 μs was selected to provide the best signal to noise ratio.

The circuitry comes equipped with pile-up rejection and pole-zero cancellation for eliminating undershoot following the first differentiating network. Pole-zero cancellation is achieved by adjusting the magnitude of a shunt resistor in the circuit until compensation is achieved.

The multi-channel analyzer receives the analogue signal from the amplifier, converts it to a digital signal, assigns the signal a channel number, and accumulates a spectrum in its memory. The MCA used in these experiments was an Ortec "Ace", IBM PC computer based system with emulation software. The computer based system provides convenient data storage on an IBM PC for further manipulation. It also features a line spectral display of acquired data and several computational analysis options such as spectrum stripping and comparison of two spectra.

The analogue to digital converter (ADC), is of the successive approximation type, i.e., comparators are used to successively re-estimate the pulse amplitude until agreement between the analogue and digital signal is in agreement. The successive approximation ADC is fast, the dead time being less than 25 μs. The dead time is fixed for this successive approximation ADC as opposed to the Wilkinson ADC in which dead time increases linearly with channel number. The greatest disadvantage associated with a successive approximation ADC is poor linearity. However, complex circuitry incorporated in the MCA has improved the linearity to less than ± 0.05% integral nonlinearity and less than ± 1% differential nonlinearity.

The relative efficiency of the detector is 15% at 1.33 MeV. The relative efficiency is defined as the ratio of the absolute detector efficiency for a point source located 25.0 cm from the center of the front surface of the detector to the absolute efficiency for a 3x3 NaI(Tl) scintillation detector in the same configuration. The relative efficiency is a function of energy, decreasing exponentially with increasing energy and decreasing rapidly at lower energies thereby displaying a maximum efficiency at some intermediate "knee" energy.

Detector Response

The radiation field that is incident on the detector is not reproduced exactly in the spectrum measured by the detector. There are several sources of measurement error in the detector system. The detector efficiency is one such source of error and the spectrum can be corrected as was discussed previously. Imperfect energy resolution is another such contribution resulting from statistical spread in the number of charge carriers, variations in charge collection efficiency, and electronic noise. These contributions lead to a Gaussian type spread in the response characterized by the full width at half maximum, Γ. The response at channel i from N_i photons with energy lying in channel j is given by

$$D(E_i)dE_i = \frac{N_i}{\sigma_j \ (2\pi)^{1/2}} \quad \exp\left[\frac{-(E_i-E_j)^2}{2\sigma_j^2}\right] dE_i \qquad [52]$$

where $\sigma_i^2 = \Gamma_i^2/ \ln(256)$

The detector response is mathematically determined by convoluting the incident spectrum with the detector response function

$$N(E) \ dE = \int R(E,E')S(E')dE' + \epsilon(E) \qquad [53]$$

where the response function, $R(E,E')$, is the probability that a photon of energy E' will produce a count with energy E, $S(E')$ is the true scattered spectrum, and $\epsilon(E)$ is a random error function.

If the response function were strictly a result of the energy resolution, then

$$N(E) = \int \frac{1}{\sigma(E') \ (2\pi)^{1/2}} \exp\left[\frac{-\ (E'-E)^2}{2\sigma(E')} \right] \ s(E') \ dE' \qquad [54]$$

$$\text{or } R(E,E') = \frac{1}{\sigma(E') \ (2\pi)^{1/2}} \ \exp\left[\frac{-\ (E'-E)^2}{2\sigma(E')} \right]$$

For a HPGe detector the energy resolution over the typical range of scatter is less than 1 keV and since the MCA channel width used was .689 keV, there is very little spread in the spectrum and deconvolution would have little effect on the spectrum.

The response function is only partially determined by the energy resolution. In addition it is necessary to consider the possibility that a photon or its secondary radiation escapes the detector. This will result in an erroneous energy determination. For example, if a photon interacts in a detector by Compton scattering, only part of its energy is transferred to an electron. It is likely that the energy transferred to the electron will ultimately be collected by the detector, but the scattered photon may likely escape. The result is a photopeak at the incident photon energy, E_0, and a lower intensity continuum at lower energies particularly below the Compton edge (corresponding to the maximum energy that can be transferred to an electron in Compton scattering for a photon of energy E_0). The detector response is a function of the photon energy, the direction of the photon, and the orientation of the detector to the photon direction. Since these geometric factors change as the flaw location varies, the response function also changes with flaw location. This is particularly true when the detector is very close to the scattering object as it was in this report.

The detector response to the radiation field scattered from a centrally located hole in a 2.5 cm aluminum test sample was calculated with a Monte Carlo program and is shown in Figure 36. This calculated spectrum shows the essential characteristics of actual measured spectra, i.e., two peaks resulting from singly and multiply scattered

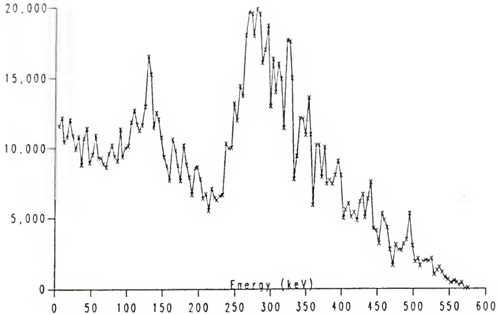

Figure 36. Calculated detector response to total scattered radiation field from central hole.

gamma-rays and the exponential decay with increasing energy.

A Monte Carlo program was also written to calculate the single scattered spectrum corrected for detector response. The single scattered spectrum is much easier to calculate than is the total, singly and multiply scattered spectrum. The program simulates radiation transport in both the sample and the detector. The energy deposited in the detector is used in scoring a particle and determines the scattered photon energy spectrum plotted in Figure 37. These differential spectra constitute the differential spectra, $\underline{Ds}$ that are used in the Least squares method for problem inversion (see equation 36).

Unfolding is a problem not unlike the inverse transport problem discussed earlier. The detector response is the solution to the Fredholm integral (equation 53) and the corresponding matrix solution for the response vector is of the form $\underline{N} = \underline{R}\ \underline{S} + \underline{\epsilon}$. The procedure is to find an unbiased vector estimate $\underline{S}'$ for the vector $\underline{S}$ [32]. The best linear estimator can then be calculated from

$$\underline{S} = [\ (\underline{R}^T\underline{V}\quad \underline{R})^{-1}\ \ \underline{R}^T\underline{V}^{-1}] * \underline{N} \qquad [55]$$

where $\underline{V}$ is the variance matrix of the vector $\underline{S}$

$$\underline{V} = E[\underline{\epsilon}\ \underline{\epsilon}^T] = E[(\underline{S}-E[\underline{S}])(\underline{S}-E[\underline{S}])\ ] \qquad [56]$$

$$= \{0 \text{ when } i = j,\ \ \sigma_i \text{ otherwise}\}$$

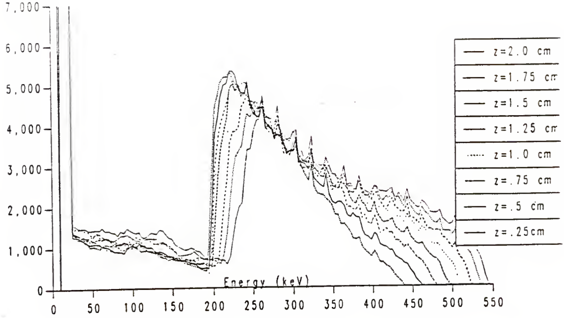

Figure 37. Calculated detector response to singly scattered radiation field from eight hole locations.

Detector Position

Just as the differential spectrum varies with hole location because of the change in the angle subtended by the detector, it will also vary as the detector is moved with respect to the sample. Figure 38 shows the once-scattered DGS for three detector positions. The detector surface is 2 cm from the sample center and the detector axis intersects the sample axis at an angle of 90°. As the angle of rotation increases, the scattered spectrum shifts to lower energies. In addition, the intensity is greater for lower angles of rotation. The figures are all normalized to a maximum of 20,000 counts, but the ratio of intensities is 25:19:41 as theta goes from 45°, 90°, and 135° respectively. This might suggest that without other limitations, it might be desirable to increase theta since the single scattered spectrum is stronger.

The spatial resolution is strongly effected by the detector position. It is estimated by a simple relationship derived from the geometry of the experiment. If a flaw located along the illuminated chord is moved along that chord, the azimuthal angle that corresponds to the single scattered ray connecting the flaw and a point on the detector will vary. If the point on the detector is projected onto the illuminated chord (see Figure 39), the distance between the flaw and projected point is

$$s = \frac{\eta}{\tan\Theta} = \text{resolution} \qquad [57]$$

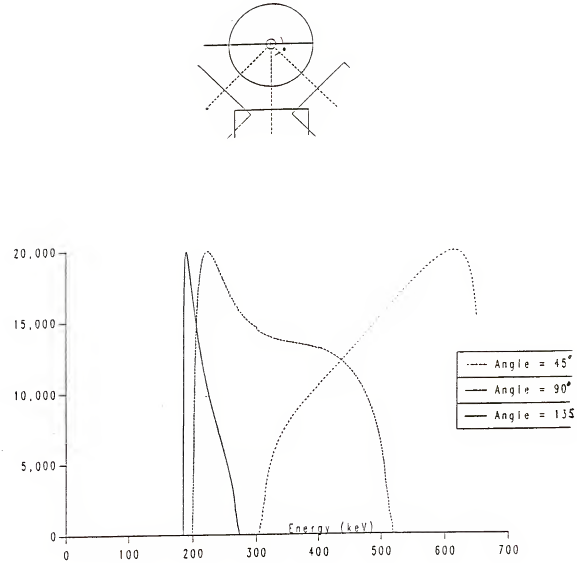

Figure 38. Single scattered differential spectrum from three detector locations in a 2.5 cm test specimen for a 0.25 cm central hole and a 4.53 cm detector.

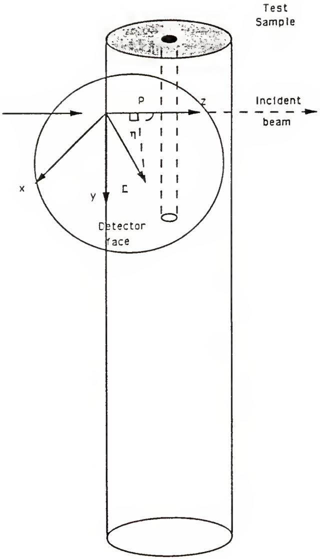

Figure 39. Projection of a point onto the illuminated chord.

where η is the normal distance from the primary beam. The derivative of s with respect to Θ will give the resolution, δs, as a function of Θ and the energy width resolved by the detector, ϵ. But we also know from equation 31 how energy changes with Θ so that

$$\frac{\delta s}{\eta} = \frac{\epsilon}{(E_0^2/511)} \quad \frac{[1 + E_0/511\ (1-\cos\Theta)]^2}{\sin^3\Theta} \qquad [58]$$

This function is plotted in Figure 40 for $E_0 = 661.6$ keV. It is obvious that at $\Theta \sim 90°$, δ is smallest and resolution is at its best. The effort of this improved resolution at 90° is evident in plots at the single scattered spectra for 3 flaws at three locations measured at these three detector angles. When Figures 41 and 42 are compared with Figure 10, it is observed that the energy range of the single scattered spectra changed more with hole location. Since it is the shape and range of the DGS that is utilized to distinguish flaw locations, it is highly desirable to achieve optimum resolution. If ϵ corresponds to a channel width of .689 keV, the fractional resolution is 0.00423 and 0.00433 at 0° and 45° respectively, whereas at 135° it is as high as 0.0234. This explains the narrow range of the differential spectrum for the case where the detector is located at 135°. Because of this poor resolution, it would be difficult to distinguish flaws that are close together or flaws of similar sizes. Therefore it is necessary to go to smaller angles of revolution.

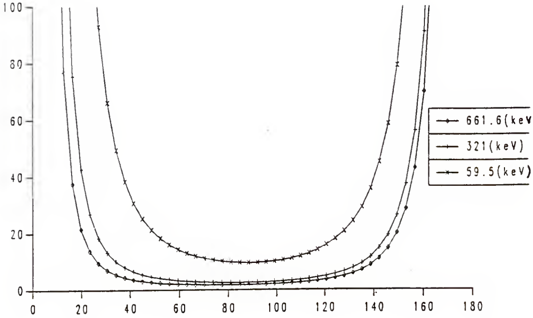

Figure 40. Fractional resolution function.

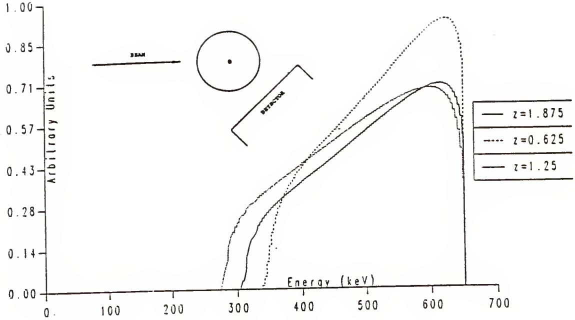

Figure 41. Ideal single scattered differential spectra for a 0.25 cm hole located along the illuminated chord at three distances from the beam point of entry.

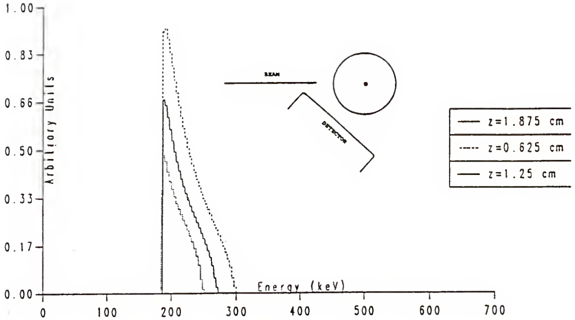

Figure 42. Ideal single scattered differential spectra for a 0.25 cm hole located along the illuminated chord at three distances from point of entry.

Another factor that might favor placing the detector at smaller angles of revolution is the separation of the multiple and single scattered spectra. Since at lower angles of revolution the detector intercepts single scattered gamma-rays with higher energies the single scattered spectrum will lie closer to the upper end of the energy scale. As a consequence of this upward energy shift, there will be less overlap between the single and multiple-scattered spectrum. Figure 43 shows the once and twice scattered spectra for a detector located at 45°. There is only a slight overlap between 300 keV to 500 keV. This shift is more noticeable in plots of the multiple scattering factor. Figures 44, 45, and 46 show how the multiple-scattered factor changes with the angle of revolution. For very high angles of revolution the multiple scattering factor is large showing a minimum at energies midway between the maximum and minimum single scattering energies. For low angles of scattering angle, the multiple scattering factor is much smaller over most of the applicable energy range and asymptotically approaches 1 at high energies. Yet another argument that might be advanced in support of going to lower detector angles is that it may be possible that the lower continuum of the response function may not overlap the range of single scattering. If this is true, the single scattered spectrum would not be significantly altered by the detector response function. The possibility of such a separation is improved for higher scattering energies

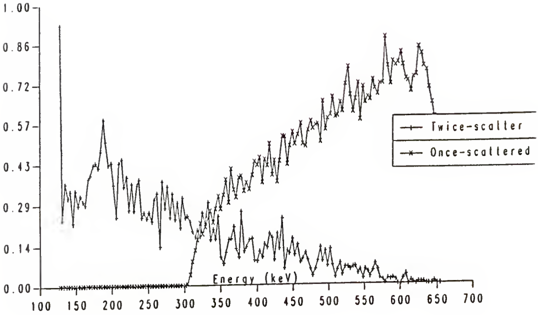

Figure 43. Monte Carlo calculated once and twice scattered spectra for a 0.25 cm central hole. Detector: x = 2.0, z = 3.25 cm, angle = 45°.

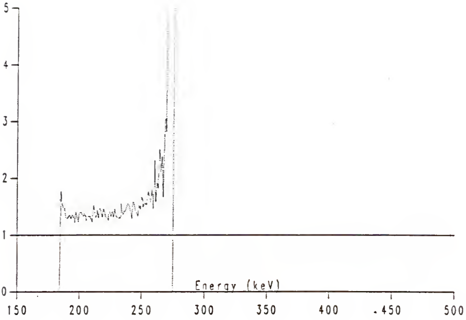

Figure 44. Multiple scattering factor for a 0.25 cm central hole. Detector: x=1.0, z = -.75 cm, angle = 90°.

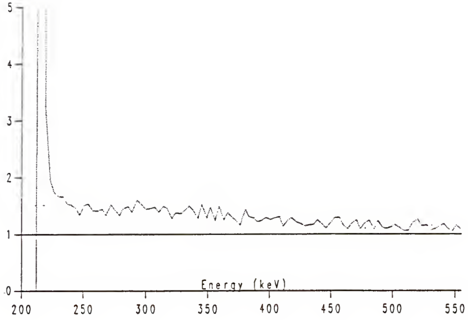

Figure 45. Multiple scattering factor for a 0.25 cm central hole. Detector: x= 2.0, z = 1.25 cm, angle = 90^0.

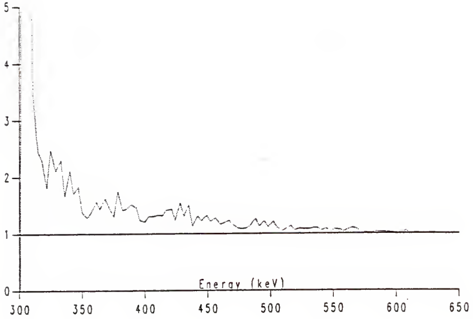

Figure 46. Multiple scattering factor for a 0.25 cm central hole. Detector: x = 2.0, z=3.25 cm, angle = 45^0.

because the gap between photopeak and Compton edge increases with the energy of the photopeak, Eo.

$$E_{gap} = \frac{E_0}{1 + 2\ Eo/511} \qquad (E_0 \text{ in keV}) \qquad [59]$$

Efficiency is another important factor to consider. As was discussed before, efficiency drops exponentially below a knee energy of about 120 keV. Therefore even if as many photons scattered into the detector located at 45° as at 90°, the detector would record fewer photons. This could be important particularly for small holes where scattering in the region of the hole is a rare event. A loss in efficiency means that the experiment must be run longer for a given source. Compton scattering tends to favor forward directions to slightly compensate for this loss.

A trade-off must be made in all these factors to achieve an optimization of spatial resolution, efficiency, and multiple scattering. The measured spectra showing the detector response at two angles of rotation, 45° and 90°, are presented in Figure 47. The experiments conducted in this report were done at an angle of 90° because of the good spatial resolution, adequate efficiency, low multiplication factor, and simplicity.

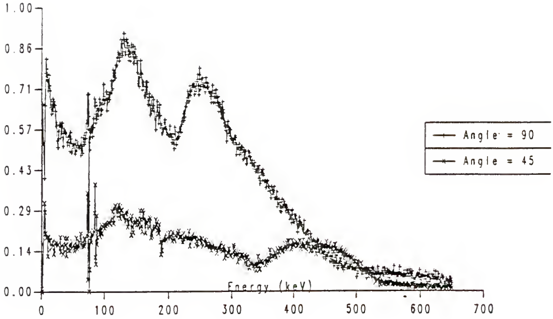

Figure 47. Comparison of DGS for two detector positions.

CHAPTER 7
RESULTS AND DISCUSSION

The Detection of Flaws

The DGSS technique has displayed a unique capability for detecting flaws both on and off the illuminated chord. The sensitivity of the system for flaw detection results from the source size, the shielding of the detector from interfering background radiation, the duration of the experiment, the size and location of the flaw, and the size and location of the detector. These factors have all been analyzed in preceding discussions.

The source should be as large as possible and is collimated into a well-defined beam. It should be properly shielded since extraneous radiation picked by the detector only degrades the statistics of the experiment.

The fractional variance is almost inversely proportional to both the square root of the accumulation time and the size of the flaw [see equations 45 and 47]. Large flaws are therefore easier to detect than are smaller flaws. In addition flaws are most readily detected when they lie along the illuminated chord because first order scattering takes place there. However, flaws that are located deep within the test sample may be more difficult to detect, particularly if the characteristic dimension of the test sample is more than a few mean paths thick. This is because the differential spectrum may be greatly attenuated by increased scattering.

The detector should be placed close to the sample to intercept as many scattered photons as possible. It was noted that flaws located between the illuminating beam and the detector are easier to detect. An array of detectors surrounding the test sample could ensure that the flaw always lies between the illuminated chord and at least one detector.

Appendix B contains the results of the study to assess the sensitivity of the system for detecting different sized flaws at various locations in an otherwise solid aluminum cylinder. Each figure gives both the geometry of the experiment together with the accumulation time and the probability P_{50} that 50 consecutive channels represent statisticly significant data. The 0.75 cm diameter hole is readily detected with a probability of approximately 1 even for short experiments where the flaw lies off the illuminated chord. The smallest flaw, 0.1 cm, was more difficult to detect. A differential spectrum collected in 17 hours for a 0.1 cm hole not on the illuminated chord could not positively indicate a flaw whose scattered photons span an energy range of 34.5 keV. For the same flaw located on the illuminated chord the probability can be as high as 1.0. This does not mean to imply that flaws smaller than 0.1 cm cannot be detected off the illuminated chord. It merely suggests the capabilities for the current experimental set up. This report did not attempt to determine the ultimate spatial resolution.

The system was also capable of detecting with probability near 1, flaws implanted on the inside wall of the steel pipe test sample, i.e., outer and inner wall thinning, a 0.25" diameter pit, a 0.5" diameter pit, and a 0.25" wide gouge. The ability to detect the flaws varied with their position, though it should be noted that flaws not on the incident beam path were detected.

Finally, when there is more than one flaw within the sample, it may be difficult to resolve individual flaws. This is particularly true when one or more flaws are located on the illuminated chord and others are not. The signal from flaws on the illuminated chord is much stronger than from others; the differential spectrum for a flaw on the illuminated chord is 10 to 100 times larger depending on the position of the flaw with respect to the detector.

When two or more flaws lie on the illuminated chord, it is more feasible to resolve them. Figure 48 shows the DGS obtained for the case of three flaws located on the illuminated chord. Also plotted in the figure, for comparison, is the DGS for a single flaw (normalized to the same peak value) located at the center. The presence of the additional flaws has altered the DGS showing that it is possible, with improved experimental statistics, to resolve the three individual flaws.

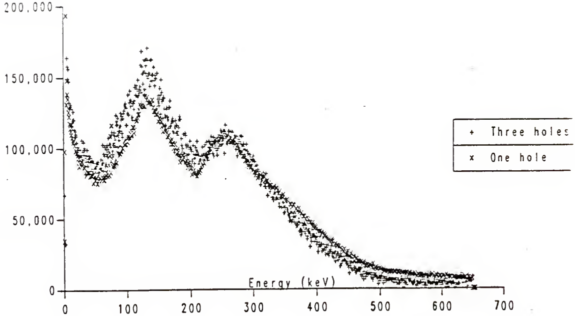

Figure 48. The Differential spectrum for three flaws together with the spectra from one central hole.

Determination of Flaw Location

The measured differential spectra for flaws will vary with the flaw location. It is this dependency that makes possible the determination of position from the differential spectrum. The differential spectra for a hole located at three positions along the illuminated chord are shown in Figure 49. The DGS for the hole nearest the point of incidence spans a higher energy range than does the DGS for a central hole, whereas the DGS for the hole nearest the exit point spans the lowest energy range. In comparing this figure with Figure 10 for scattering in a perfect detector, it is seen that the shapes of these curves have been modified by the presence of multiple scattering in the sample and even more importantly, by the response of the detector. The detector efficiency drops off almost exponentially with increasing energy which accounts for the fact that the measured spectra "trail off" at higher energies rather than sharply decreasing to zero.

The location of flaws not on the illuminated chord also affect the differential spectra. These spectra will shift in energy just as they did for flaws along the illuminated chord. However, these variations are more difficult to perceive since the statistical variances are much larger. Figure 50 shows the differential spectra experimentally obtained for two locations on opposite sides of the illuminated chord. Flaws located in the region

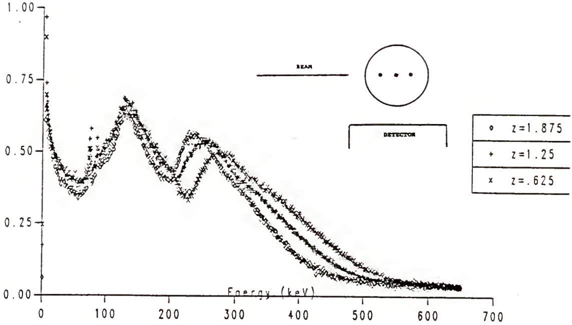

Figure 49. Differential spectra for three flaw locations along the illuminated chord.

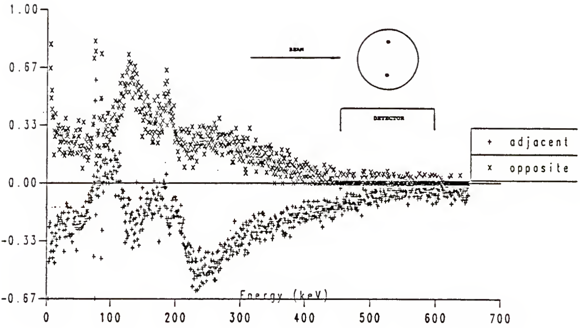

Figure 50. Differential spectra for two flaws not on the illuminated chord. Flaws in both the region adjacent the detector and opposite the detector are shown.

behind the illuminated chord, across from the detector, are most difficult to detect and result in the largest statistical variances since these flaws are detected entirely by photons that have scattered at least twice.

Appendix B also presents experimentally obtained differential spectra for the pipe experiments. Again, the DGS is highly dependent on the flaw location. For example, when the beam lies along the illuminated chord, a strong positive single scattered peak is evident in the differential spectra, and is notably absent when the flaw lies off the illuminated chord. In fact when the flaw lies in regions where not only the uncollided beam does not pass through the flaw, but even once-scattered radiation cannot pass directly through the flaw into the detector, the differential signal is extremely weak. The flaw lies in a "blind" spot for this particular detector location. It is necessary for photons to undergo at least two scattering interactions in the sample of which one either occurs in the flawed region or scatters a photon that passes through the flawed region into the detector. As the pit is rotated so that once collided photons can pass through the flaw into the detector, the differential spectrum shows a more intense negative spectrum. Rotating the pit even farther so that it intersects the uncollided beam on the back side of the pipe near the point of exit, the spectrum rapidly becomes more positive. These variations are shown in Figure 51.

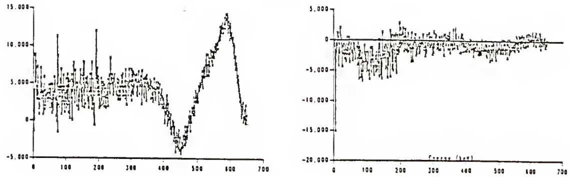

a) uncollided beam passes through flaw near the beam point of incidence.

b) uncollided beam and once-scattered beam cannot pass directly through flaw into detector.

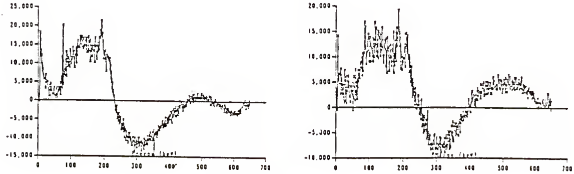

c) uncollided beam does not pass through flaw but once-scattered radiation does.

d) uncollided beam passes through flaw near the beam point of exit.

Figure 51. Variation in differential spectra with pit location in pipe sample.

Determination of Flaw Size

The size of the flaw will affect both the shape of the DGS and its intensity. It is the intensity that is the more sensitive gauge of the flaw size. Figures 52, 53, 54, and 55 show the DGS for four different sized flaws placed in the center of the test spectrum. As the size increases, more photons scatter from the flaw into the detector. It is reasonable to expect then that the area under the differential spectrum in the range of single scatter should be a good indication of the flaw size. Table 2 shows both the maximum intensity and the integral of the differential spectrum over the range of single scattering for the four flaw sizes: 0.1 cm, 0.25 cm, 0.5 cm, and 0.75 cm. Also shown in the table is the volume of the flaw/beam intersection. As expected, there is good agreement between these values. For small flaw sizes where the statistical variances are larger, the discrepancy between the values is more significant.

Table 2.
Comparison of integral of differential spectrum to the volume of the beam/flaw intersection

Flaw Diameter (cm)	Relative Volume of Intersection	Relative Maximum Intensity	Relative Integral of DGSS
0.75	1.0	1.0	1.0
0.50	0.624	0.611	0.577
0.25	0.193	0.190	0.136
0.10	0.0322	0.0454	0.0451

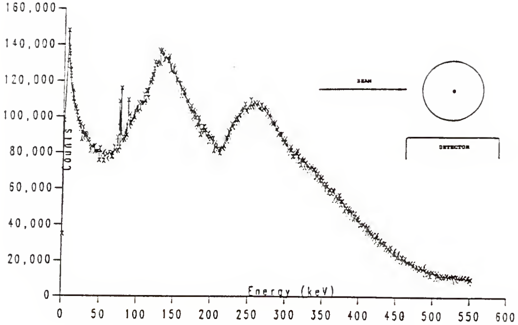

Figure 52. Differential spectrum for 0.75 cm centrally located hole.

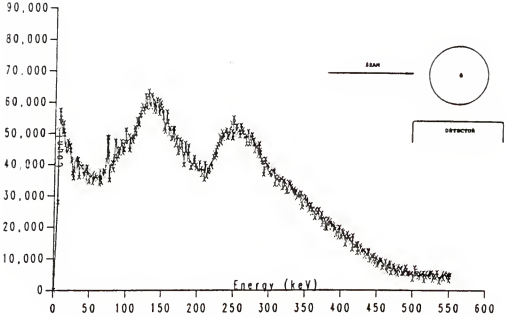

Figure 53. Differential spectrum for 0.50 cm centrally located hole.

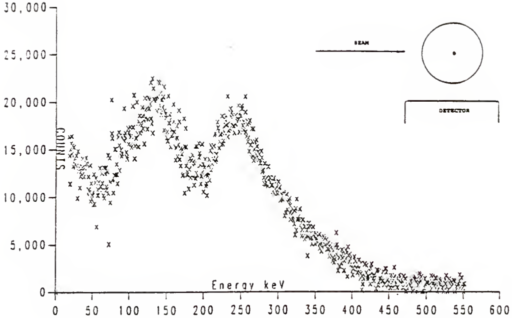

Figure 54. Differential spectrum for 0.25 cm centrally located hole.

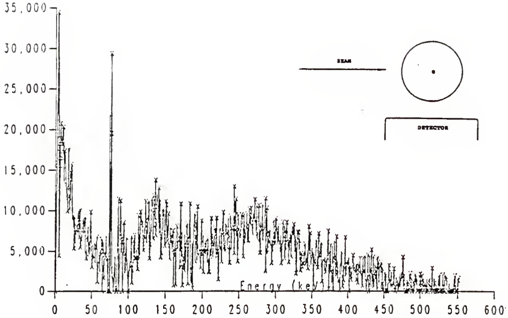

Figure 55. Differential spectrum for 0.10 cm centrally located hole.

The experiment utilizing the tapered central hole which was used to test for wall thinning in pipes, generated excellent data for measuring changes in wall thickness. For example three differential wall thicknesses were considered: 0.254 cm, 0.508 cm, and 0.762 cm. Again the change in wall thickness should be proportional to the area under the DGS curves. This is apparent when the ratio of the areas under respective DGS curves is calculated, i.e., 0.513:1.0:1.51. This ratio agrees well with the ratio of wall thinning, 0.5:1.0:1.5.

When a pit is implanted in a pipe and the beam is passed through the pit, the pit's size can be determined by both the intensity and shape of the DGS. The intensity will indicate the depth of the pit along the beam since more single scattering will take place in the deeper pit. The shape of the DGS will indicate the diameter of the pit. Figures 56, 57, and 58 show the differential spectra for a 0.635 cm diameter pit, a 1.27 cm diameter pit, and a long 0.635 cm wide gouge. Note that the DGS for the narrow pit is positive over most of the range of the spectrum. The other two spectra drop below zero between about 300 keV to 500 keV. The difference between the spectra for the two sized pits (the DGS for the 1.27 cm pit minus the DGS for the 0.635 cm pit) is plotted in Figure 59. The DGS for the larger pit is negative over a larger range of the spectrum. The reason for this is seen in Figure 60, a diagram of the

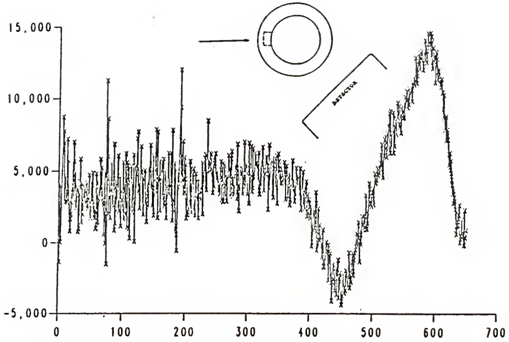

Figure 56. Differential spectra for 0.635 cm diameter pit on inside wall of pipe.

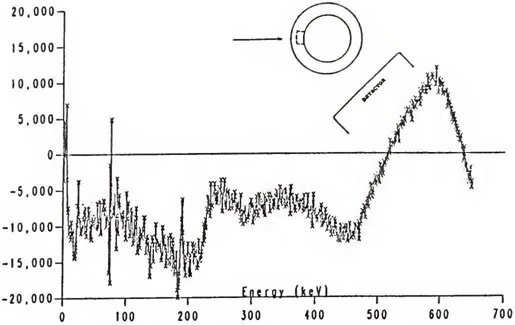

Figure 57. Differential spectra for 1.27 cm diameter pit on inside wall of pipe.

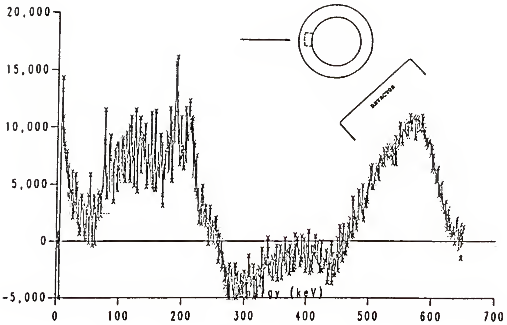

Figure 58. Differential spectra for 0.635 cm wide gouge on inside wall of pipe.

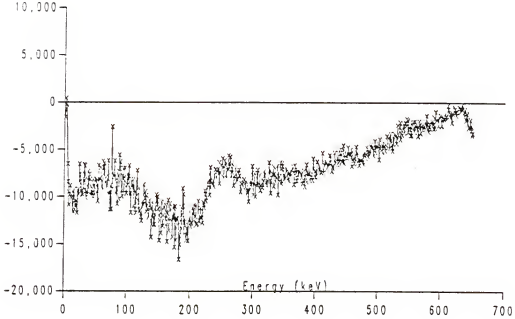

Figure 59. The difference between the DGS for a 1.27 cm diameter pit, and a 0.635 cm diameter pit. Both pits lie along the illuminated chord nearest the point of incidence.

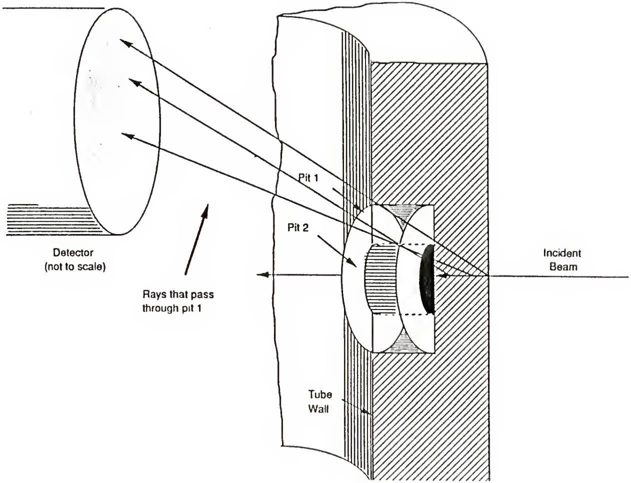

Figure 60. Diagram of pipe, pit, and detector geometry showing those scattered gamma-rays contributing to the differential spectra.

pipe, pit, and scattered photons contributing to both differential spectra. The amount of single scattering occurring in the flaw region will be similar for both samples since the volume of intersection between the beam and pit is nearly the same for both. However, photons scattering in the region between the point of incidence and the flaw will see less attenuation in the sample with the larger pit. The same is true for the case of the gouge. The DGS for the gouge is more negative over a wider energy range than for the small pit, but less negative over a narrower energy range than for the large pit.

CHAPTER 8
CONCLUSIONS

The scattered radiation field emerging from a test object that is illuminated by a beam of gamma rays contains a wealth of information describing the density distribution of the object. In the DGSS technique, the portion of this field incident on a solid state detector is measured with very fine energy resolution and transformed into an energy spectrum. The measured spectrum from a reference sample of known density distribution is compared with the scattered radiation spectrum from an unknown test sample and the resulting differential energy spectrum is spectrally analyzed to characterize the size and location of the flaw. The differential spectrum contains mostly that information that characterizes the flaw. All photons that do not scatter in, or pass through the flaw are effectively stripped away in the difference. This also reduces the level of multiple scattering in the single scattering energy range of the differential spectrum. These attributes are desirable in simplifying the analysis of the differential spectrum.

Radiation transport in media is well described by transport theory. Equations describing radiative transport have been developed to a point where the differential spectrum incident on the detector face can be calculated from both the Monte Carlo and discrete elements techniques. There is excellent agreement between these two methods providing a check on the algorithms developed for this research. These techniques are employed in computer codes so that variations in the DGS with detector position, flaw location, and flaw size can be numerically modeled.

Methods of inverse transport were also developed. By inverse transport methods it is meant that the objective of solution is to calculate the density profile from a known source and known scattered spectrum as opposed to the more frequent forward problem of calculating the scattered spectrum from a known source and known material properties.

The equation describing the forward problem can be discretized by energy and location of scattering along the illuminated chord. It was pointed out that if there were no statistical uncertainty associated with the measured spectrum the problem could be conveniently inverted through simple matrix inversion. But, because of the inherent uncertainty associated with spectrum measurements, less direct techniques must be employed. One such technique developed for this report was the method of least squares fit. For this technique the illuminated chord was segmented into pixels and the scattered spectrum was calculated for each pixel. This set of differential spectra formed a set of describing functions characterizing the variation of the differential spectra with flaw location. The function or combination of functions that agreed most closely with the measured differential spectra by minimizing a least squares error parameter determines the most probable density distribution.

The DGSS technique has amply demonstrated a capability for detecting, locating, and sizing flaws. Flaws as small as 1 mm could be detected by experiment even when the flaw lay off the illuminated chord and smaller flaws may be detectable with an improved experimental set-up. A larger source can improve the statistics of the differential spectra. However, larger sources were not acquired for this phase of the research because of the excessive time delay associated with licensing, shipping, and shielding a new source. This report in no way attempted to determine the ultimate resolution and accuracy achieveable with the DGSS probe.

The sensitivity for detecting flaws varies with the size and position of the flaw in the test sample. Flaws located along the illuminated chord were much easier to detect since their differential spectra were 10 to 100 times greater than those spectra resulting from flaws off the illuminated chord.

The location of flaws along the illuminated chord can be determined by first calculating the DGS's (corrected for detector response) for various flaw positions and then comparing the measured response with the calculated DGS's and determining the combination of such calculated DGS's that most accurately agrees. It was possible to determine the location of a 0.75 cm flaw within .25 cm. This resolution may be further improved by improving the accuracy of the calculated DGS's corrected for detector response.

Several experiments were conducted to demonstrate how the DGS varies with flaw location. A flaw implanted in a solid aluminum sample was placed in a number of locations in the sample to show how the sensitivity varied with flaw location. As a more practical example, these sensitivity experiments were also conducted on pipe samples. It also showed that for only one detector location, there may be "blind" spots in the sample where the detector is unable to detect flaws. This problem can be rectified by viewing the sample from more than one detector location.

The size of the flaw along the illuminated chord can be estimated from the area under the DGS in the region of single scattering. Strictly speaking, this determines the volume of the part of the flaw that lies on the illuminated chord. It was shown that this could quite accurately predict the size of cylindrical holes in a solid rod, or be used in estimating the amount of wall thinning in pipes.

The DGSS technique is not without limitations. For example, it was noted earlier that DGSS is sensitive to bulk density variations and not to surface effects. Fine microcracks for which little or no air gap exists between crack surfaces may go undetected with this technique. If ultrasonics can be used in a particular application and it is desired to inspect for such flaws, the DGSS technique would obviously take a back seat.

Some NDE applications require very high scan rates. For example, it was mentioned in Chapter 1 that when inspecting boiler tubes, a linear scan rate of 15.2 m/min is necessary. Results of experiments show that with a 0.5 Ci Cs-137 source, a 0.635 cm diameter, 0.318 cm deep pit located on the illuminated chord can be detected in as little as 100 seconds. It is estimated that if the size of the source were increased to 20 Ci, the same flaw could be detected in only 2.5 seconds. Of course, flaws not on the illuminated chord are not so easily detected, but by utilizing more detectors, the efficiency may be increased to about this same level. Assuming the flaw could be detected in 2.5 seconds, it would be necessary to examine the tubes in intervals longer than 0.63 m to obtain the needed scan rate. This does not take into account the time needed to move the source and detector, which could be quite large. Typically, ultrasonics can detect wall thinning with an accuracy of 0.127 mm at the same scan rate in intervals between 0.3 m and 1.5 m [33]. It is unlikely that the DGSS technique could achieve scan rates superior to ultrasonics.

The ability of the DGSS technique to detect density perturbations from a reference state is contingent on the existence of a reference state. For example, it is difficult to recognize a reference state when the object of scrutiny is a weld, i.e., welds are highly nonuniform. However, it may be possible to monitor a weld through its lifetime if the accepted reference state is the weld at the time it is placed in service. The differential spectrum from this reference state can be stored on computer and used for comparison at later periodic inspection times.

As mentioned earlier, the detection of flaws in thick samples or the detection of small density perturbations may be difficult. When the test object is more than a few mean free paths thick, locating flaws is made difficult by multiple scattering which may be quite large in such samples. The spectrum will shift to lower energies and photon absorption will become increasingly important so that fewer scattered photons reach the detector and the sensitivity for detection will decrease. This report did not attempt to determine the extent of these limitations for flaw detection.

The probe can yet be improved by increasing the source strength and improving the shielding of the source. Furthermore, the use of a large position sensitive detector can greatly improve the sensitivity of the detector. Figure 61 shows a diagram of such a detector system that might be used. The individual detectors can be simply cylindrical or constructed in a variety of shapes in an effort to intercept single scattered photons that fall within a select band of energies. Such a bank of detectors would provide an increase in the overall efficiency of the system (a large number of detectors could subtend more of the scattered radiation field) and would provide more detailed information about how the field varies with position, thereby increasing the spatial resolution.

As was mentioned earlier, the differential spectrum from a flaw not on the illuminated chord is several orders of magnitude smaller than the differential spectrum from a flaw along the illuminated chord. This makes detecting flaws not on the illuminated chord a difficult task in the presence of a flaw along the illuminated chord since its contribution to the differential spectrum may be difficult to distinguish from statistical variations. An efficient position sensitive detector composed of small detector elements may remedy this problem since for a pair of flaws there may be a detector position for which the scattered spectrum from the two flaws do not significantly overlap in energy range.

The ability of the probe for detecting far from the surface flaws in complex objects with a modest exposure to the object, makes it an attractive means for detecting flaws in irregular components, composites, honeycomb structures, and biological tissues as well as other more traditional

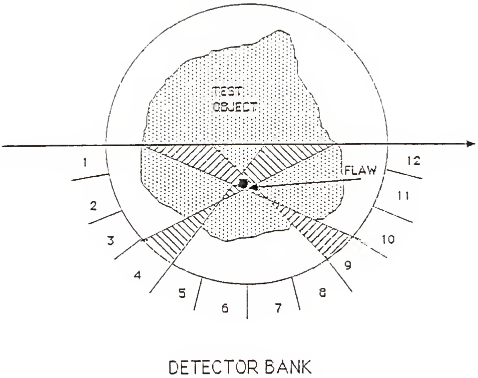

Figure 61. Diagram of position sensitive detector. The figure shows one half of a system of detectors for detecting flaws. Also shown is the range of scattering angles intercepted by the flaw and two detector positions.

applications. Such improvements as mentioned above will be incorporated in future development of the DGSS probe. These improvements will further enhance the usefulness of the probe for industrial and laboratory applications.

APPENDIX A
MONTE CARLO CALCULATIONS

Monte Carlo is a stochastic technique for solving complex problems. The basic procedure is to track a particle from birth to death, simulating its interactions by sampling from probability distributions that describe each interaction process. If a large number of particles are monitored, their behavior on a hole approaches the average behavior expected from an infinite number of particles.

Consider the case of a cylindrical sample with a photon beam passing through its center as was shown in Figure 39. The beam point of incidence is taken as the coordinate origin $x = 0$, $y = 0$, $z = 0$ and the beam has direction cosines $\alpha = 0$, $\beta = 0$, $c = 1$ with respect to the x, y, and z axis, respectively. A cylindrical coaxial detector has a circular face with diameter, D, with unit normal vector having direction cosines $\alpha_D = -1.$, $\beta_D = 0$, and $c_D = 0$, and whose center is placed at $x\ D/2$, $y = 0$, and $z = D/2$.

A photon travelling along the illuminated chord can interact anywhere along this chord or may pass through the cylinder entirely without interaction. The probability of undergoing an interaction along the illuminated chord at less than a distance, s, is given by

$$P(s) = 1 - \exp(-\int_0^s ds'\ \Sigma_t(s')) \qquad \text{A.1}$$

If the medium is uniform then the path length, s, can be selected by

$$s = - \ln (r_1)/\Sigma_t \qquad \text{A.2}$$

where r_1 is a uniformly distributed random variable between 0 and 1. A path length so chosen will be distributed according to equation A.1. If the medium is piecewise homogeneous or homogeneous but discontinuous (such as in the vicinity of a hole) the solution is still attainable. The procedure is to calculate the path length, s, assuming that the particle interacts in the region surrounding the particle origin. If the particle passes into an adjacent region then the particle escapes the immediate region and is moved to the point of entry into the next region. The path length is recalculated according to equation A.2 using material characteristic of this region without changing the direction vector of the particle. The process continues until the particle interacts or escapes the region of interest.

In the case of a hole located on the illuminated chord, the particle can be forced to undergo its first scatter in the hole by sampling s from

$$s = \frac{-1}{\Sigma_t} \ln [1 - r_1(1 - \exp(-\Sigma_t D))] \qquad \text{A.3}$$

and weighting the particle by the probability of interacting in the hole:

$$w = \exp(-\Sigma_t H)(\exp((\Sigma_t d/2) - \exp(-\Sigma_t d/2) \qquad A.4$$

where H is the distance to the center of the hole and d is the diameter of the hole.

Since forcing the particle to interact in the hole increases the importance of that particle, the number of histories needed to approach the average limit decreases. This technique goes under the category of variance reduction. If the hole does not lie along the illuminated chord, variance reduction can also be incorporated by first determining the solid angle subtended by the hole and then forcing particles to scatter into or through the hole (see Figure 11 for a description of events leading to the differential spectrum). Any time the particle is forced to scatter in any particular manner the weight of the particle must be corrected.

Next the particle may undergo interactions in the sample. The probability distribution for the various interactions are characterized by the cross-sections governing them. A photon may undergo pair-production, Compton scattering or the photoelectric effect. When the energy of the source is less than 1.022 MeV (as in the case of the Cs-137 source used in this report), pair production is no longer possible. In the photoelectric effect the photon is absorbed and an electron is emitted which would generate only very low energy secondary radiation. The probability of scattering is therefore $P_s = \Sigma_{comp}/(\Sigma_{comp} + \Sigma_{pe})$ and after each collision the weight of the particle is reduced by this factor.

Since scattering in the polar direction with respect to the direction of a photon incident on a target electron is uniformly distributed, the polar scattering angle can be determined by $\phi = r_2 * 2\pi$ where r_2 is a random number generated uniformly between 0 and 1. Now the azimuthal angular distribution of scattered photons is described by the Compton cross-section and was given in equation 2. The Kahn rejection technique is used to sample the azimuthal angular distribution. This is an example of a combined composition-rejection technique applied to probability density functions, PDF's. The PDF can be viewed as a linear finite sum of probability density functions appropriately weighted.

The scattering angle may now be used to calculate new direction cosines as explained in Figure A-1. The particle is free to travel in a new direction until it interacts with the medium. After continued interaction, the particle is either absorbed, scattered into the detector, or it escapes from the system.

For $\gamma \neq 1$

$$\alpha' = \alpha \times \cos\theta + \gamma \times \alpha \times \frac{(\sin\theta \times \cos\theta)}{\sqrt{(1 - \gamma^2)}} - \beta \times \frac{\sin\theta \times \sin\varphi}{\sqrt{1 - \gamma^2}}$$

$$\beta' = \beta \times \cos\theta + \gamma \times \beta \times \frac{\sin\theta \times \cos\varphi}{\sqrt{1 - \gamma^2}} + \alpha \times \frac{\sin\theta \times \sin\varphi}{1 - \gamma^2}$$

$$\gamma' = \gamma \times \cos\theta - \sqrt{1 - \gamma^2} \times \sin\theta \times \cos\varphi$$

For $\gamma = 1$

$$\alpha' = \sin\theta \times \cos\varphi$$

$$\beta' = \sin\theta \times \sin\varphi$$

$$\gamma' = \gamma \times \cos\theta$$

Figure A.1. Calculation of new direction cosines from current direction cosines and scattering angles.

There are methods for improving the efficiency of the calculation. For example, if the particle is allowed to be absorbed in the material, the chain of calculations leading up to that point are wasted. Rather than allowing absorption, the particle is forced to scatter after each collision and the particle weight is reduced appropriately. The particle is terminated when its weight is sufficiently low.

In addition, it is extremely inefficient if particles are scored only when they escape the object and enter the detector. Instead, an estimate of the particle's contribution to the radiation field incident on the detector is made after each collision. A particle with direction $\underline{\Omega}$ scatters at $\underline{r}$ with polar angle Θ and azimuthal angle ϕ. After each scattering event the probability of scattering is calculated and the polar angle is sampled from the Klein-Nishina formula. Now the estimate is made based on the particle weight, the azimuthal angle intercepted by the detector, and the probability of escaping the object without interaction. Since the azimuthal angle is uniformly distributed, the probability of scattering into interval $d\phi$ about ϕ is appropriately, $P_\phi \, d\phi = d\phi/(2\pi)$. There may be a range of ϕ, $\phi \epsilon (\phi_1, \phi_2)$ for which the particle can scatter into a direction subtended by the detector. The detector response is estimated by

$$D(E) = w \int_{\phi_1}^{\phi_2} P_\phi d\phi \; e^{-\mu z(\underline{r},\underline{\Omega}(\phi))} \qquad \text{A-5}$$

where w is the weight of the particle after colliding at $\underline{r}$, and $z(\underline{r},\underline{\Omega}(\phi))$ is the distance from point $\underline{r}$ to the test specimen surface for a particle traveling in direction $\underline{\Omega}$.

Now suppose the direction vector, $\underline{\Omega}$, is extended from point $\underline{r}$ until it intersects with the plain containing the front surface of the detector at point (x_2, y_2, z_2). Then the range limits of the range $\{\phi_1, \phi_2\}$, will result from the inequality,

$$(y_2 - y_D)^2 + (z_2 - z_D)^2 < D^2/4 \qquad \text{A-6}$$

Or

$$\frac{(x_D - x_1)\beta'}{\alpha_D\alpha' + c_D c'} + y_1 - y_D + \frac{c'(x_D - x_1)}{\alpha_D\alpha' + c_D c'} + z_1 - z_D \leq D^2/4$$

where D is the detector diameter; x, y, z are the coordinates of the point $\underline{r}$; x_0, y_0, z_0 are the coordinates of the center of the detector face; α', β', c' are the direction cosines of the particle; and α_D, β_D, c_D are the direction cosines of the detector.

Since α', β', and c', are functions of the angles of scatter, Θ and ϕ, when Θ is determined, ϕ_1 and ϕ_2 can be calculated by solving the inequality.

Only a few particle tracks actually contribute to the differential spectrum, particularly for cases where the flaw does not lie along the incident beam path. The efficiency of the calculation can be further improved by statistical biasing. As was shown in Figure 11, only those particles that scatter into or through a hole contribute to the differential spectrum. It is reasonable then that savings in computational time can be achieved if particles are either forced to scatter into or through flaws and their weights correspondingly reduced or the particle split into two particles, one forced to scatter into or through the flaw, the other not (here again the weight of both particles must be adjusted). These techniques are used and can greatly reduce the statistical variance of the results.

At the point of collision, the polar scattering angle, Θ, is selected using the Kahn Rejection technique. Then the range of azimuthal angles that intercept the hole is determined. This is accomplished via the inequality:

$$(z_2-z_h)^2 + (x_2-x_h)^2 \leq r_h^2 \tag{A-7}$$

where x_h, y_h, z_h are the coordinates of the hole center and r_h is the hole radius. Substituting $z_2 = z_1 + cH$, $x_2 = x_1 + \alpha H$, $u = z_1 - z_h$, and $v = x_1 - x_h$ where H is the distance traveled by the particle.

$$H^2(c^2+\alpha^2) + 2H(uc+v\alpha) + u^2 + v^2 \leq r_h^2 \tag{A-8}$$

This quadratic equation has two solutions with simple physical interpretations. The particle direction will either pass through the hole, entering at $H = H_1$ and leaving at $H = H_2$ or just graze the cylindrical hole when $H = H_1 =$

H_2. The values of ϕ for which the particle just grazes the hole correspond to the endpoints of the range of ϕ, i.e., $\phi \in \{\phi_1,\phi_2\}$. Therefore if the determinant of the quadratic equation is set to zero, the resulting equation can be solved for ϕ_1 and ϕ_2:

$$(uc+v\alpha)^2 - (c^2 + \alpha^2)\ (u^2 + v^2 - r_h^2) = 0$$

where a, β, and c are functions of ϕ.

The flow of logic in Monte Carlo calculations is direct. It is best described by a flow chart as in Figures A-2, A-3, and A-4. Figure A-2 describes the Monte Carlo process for the case of a hole that lays along the illuminated chord. For this case the particle is forced to originate at the location of the hole since these particles contribute overwhelmingly to the differential spectrum.

Figures A-3 and A-4 show the flow chart for the case of a hole located off the illuminated chord. Here, at each collision the particle is weighted by the probability of passing through the hole into the detector and then scored. The particle is then split into two particles: one that interacts within the hole (if it is possible to scatter into the hole) and one that doesn't. This process continues until the particle either escapes or its weight becomes insignificant.

The Monte Carlo calculation must be terminated at some point and the decision as to just how many particle histories are to be tracked is important. If the program is

Figure A.2. Flow chart for Monte Carlo calculation of the differential spectrum from a hole located on the illuminated chord.

Legend of Symbols Used in Flow Chart

E = Current energy of particle
Eoo = Initial energy of particle
Ω =Current angular direction of particle
Ωo = Initial angular direction of particle
r = Current spatial vector of particle
ro = Initial spatial vector of particle
w = weight of particle
Nscat = Number of times particle has scattered

Θ = Azimuthal scattering angle
ϕ = Polar scattering angle
$(\phi_1, \phi_2)_{det}$ = Range of polar angles subtending the detector
$(\phi_1, \phi_2)_{hole}$ = Range of polar angles subtending the flaw
Σ_{scat} = macroscopic scattering cross-section
Σ_{total} = macroscopic total cross-section

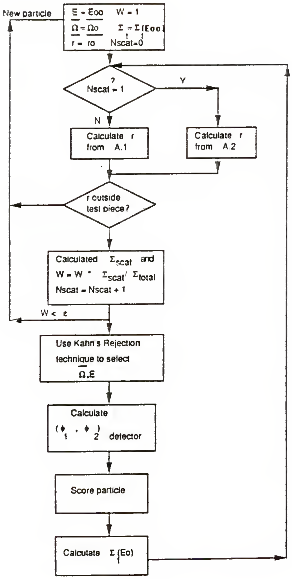
New particle
E = Eoo W = 1
Ω = Ωo Σ = Σ(Eoo)
r = ro Nscat=0
? Nscat = 1
Y
N
Calculate r from A.1
Calculate r from A 2
r outside test piece?
Calculated Σscat and
W = W * Σscat/ Σtotal
Nscat = Nscat + 1
W < ε
Use Kahn s Rejection technique to select Ω,E
Calculate (φ1 , φ2) detector
Score particle
Calculate Σ(Eo)

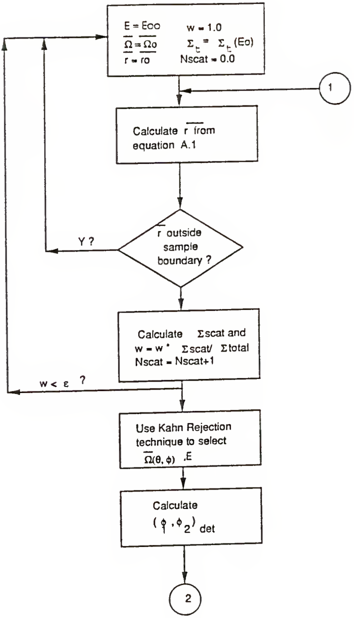
E = Eoo
$\overline{\Omega} = \overline{\Omega o}$
$\overline{r}$ = ro
w = 1.0
$\Sigma_t = \Sigma_t$(Eo)
Nscat = 0.0
1
Calculate $\overline{r}$ from equation A.1
$\overline{r}$ outside sample boundary ?
Y ?
Calculate Σscat and
w = w * Σscat/ Σtotal
Nscat = Nscat+1
w < ε ?
Use Kahn Rejection technique to select $\overline{\Omega}(\theta, \phi)$,E
Calculate
(ϕ_1, ϕ_2) det
2

Figure A.3. Flow chart for the Monte Carlo calculation of the differential spectrum from a hole not located on the illuminated chord.

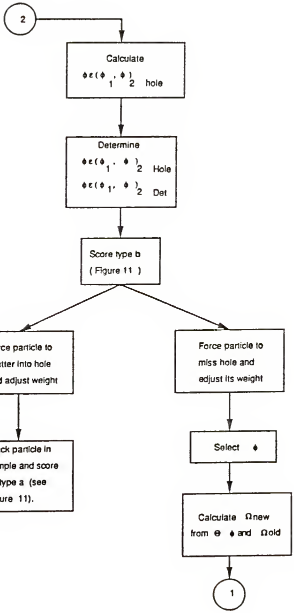

Figure A.4. Flow chart for the Monte Carlo calculation of the differential spectrum from a hole not located on the illuminated chord.

terminated too soon the calculation will show severe statistical spread. Likewise the program could be allowed to run too long unnecessarily consuming computation time.

There are a couple means by which the program user can determine when to terminate the program. At each particle iteration all calculated and initialized data are stored in a file so that the program can be stopped at any moment, the calculated spectra visually inspected, and the program may be further resumed. This allows the user to qualitatively examine the spectra for convergence.

Another technique that can be used is to record the distribution of polar angles sampled at first collision. The sampling technique used is the Kahn rejection technique which approaches analytical PDF associated with the Klein-Nishina formula for the scattering cross-section. If the sampled PDF is compared with the analytical PDF and there is good agreement, the program may be terminated. Agreement is determined by applying the chi-squared test to the two distributions.

Finally, the error of the calculation can be estimated by a result of the central limit theorem [34]. This theorem states that for N source particles and M_i events that fall within a certain energy band i, the probability that the calculated ratio of events within that band falls within the range ϵ surrounding the true average, μ can be calculated from:

$$P\left(\left|\frac{M_i}{N} - \mu\right| < \epsilon\right) = \operatorname{erf}\frac{t}{\sqrt{2}} + \flat_N \qquad \text{A-10}$$

where

$t = \epsilon N^{1/2} \sigma_e^{-2}$ and $\flat_N \rightarrow 0$ as $N \rightarrow \infty$

If a large number of histories are tracked then $\flat_N \approx 0$ and can be neglected. Now, we can specify a tolerance, ϵ, in the estimate of the average, μ, and calculate the probability, $P(|M_i/N - \mu| < \epsilon)$. It is necessary to estimate the variance, σ_e from the sample variance $\sigma_e^2 = \sigma^2/N$.

APPENDIX B
DIFFERENTIAL SPECTRA

The following Appendix presents measured Differential Gamma Spectra for various experimental configurations. Figures B.1 through B.19 are the results of the sensitivity experiments to demonstrate the ability of the system to characterize the flaw as the flaw size and location were varied. The flaw size and location as well as the live time for the experiment (for both reference and test specimen) and the probability that the differential spectrum presents statistically significant information is indicated for each figure.

Figure B.20 is the measured DGS for the case of three holes in the test sample. These three holes could not be resolved as indicated in the preceding text.

Figures B.21 through B.30 show similar spectra obtained for the pipe experiments to determine the abilities of the probe for detecting wall thinning, internal pitting, gouging, and microcracks. Figures B.21 and B.22 are the results for the tests for wall thinning whereas the other spectra show how the DGS change with the size and type of flaw.

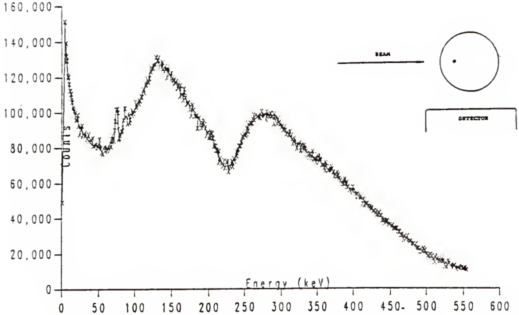

Figure B.1. DGS for a 0.75 cm flaw located at x=0, z=0.625 cm in a 2.5 cm aluminum cylinder. P_{50} = 1, T = 61234 sec.

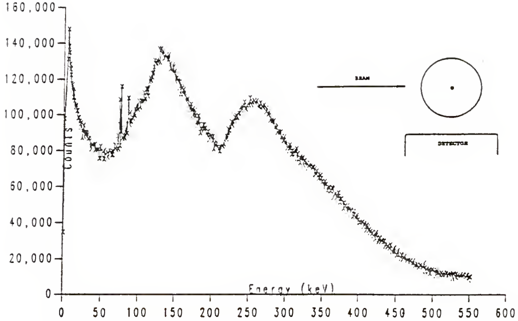

Figure B.2. DGS for a 0.75 cm flaw located at x=0, z=1.625 cm in a 2.5 cm aluminum cylinder. P_{50} = 1, T = 61234 sec.

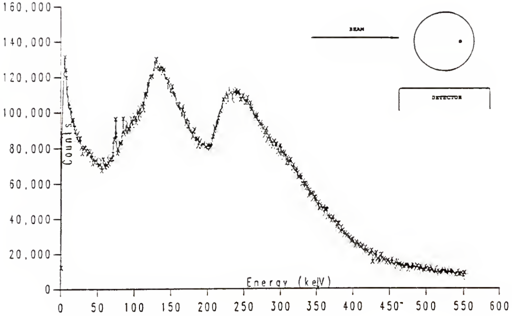

Figure B.3. DGS for a 0.75 cm flaw located at x=0, z=1.875 cm in a 2.5 cm aluminum cylinder. P_{50} = 1, T = 77912.

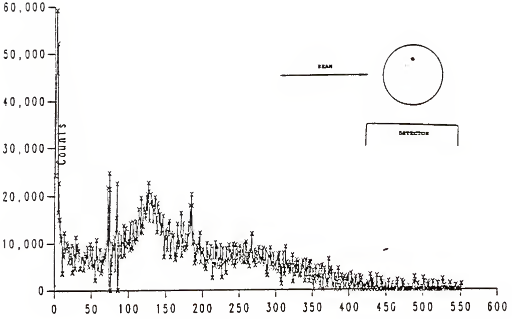

Figure B.4. DGS for a 0.75 cm flaw located at x=-.625, z=1.25 cm in a 2.5 cm aluminum cylinder. P_{50} = 1, T = 77912 sec.

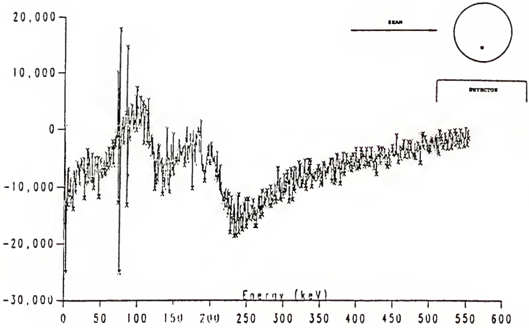

Figure B.5. DGS for a 0.75 cm flaw located at x=.625, z=1.25 cm in a 2.5 cm aluminum cylinder. $P_{50} = 1$, T = 77912 sec.

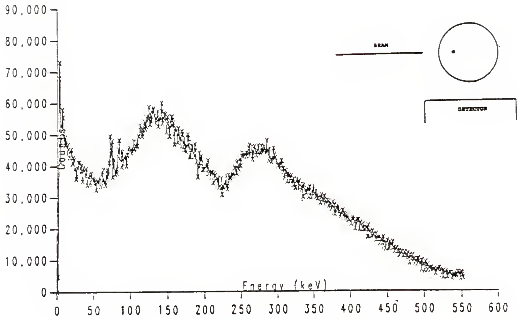

Figure B.6. DGS for a 0.50 cm flaw located at x=0, z=0.625 cm in a 2.5 cm aluminum cylinder. P_{50} = 1, T = 61079 sec.

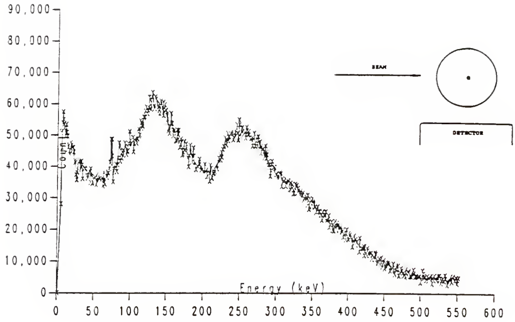

Figure B.7. DGS for a 0.50 cm flaw located at x=0, z=1.25 cm in a 2.5 cm aluminum cylinder. P_{50} = 1, T = 61079 sec.

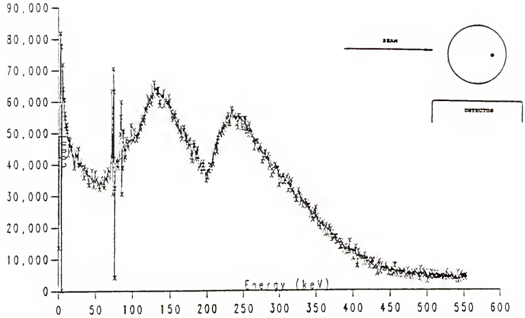

Figure B.8. DGS for a 0.50 cm flaw located at x=0, z=1.875 cm in a 2.5 cm aluminum cylinder. P_{50} = 1, T = 61079 sec.

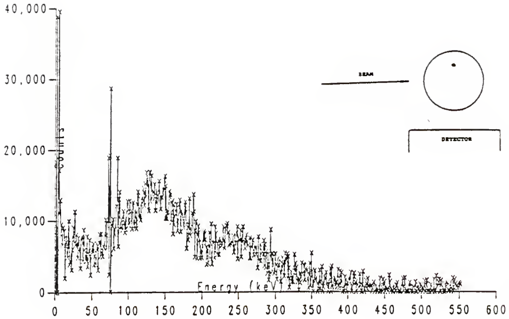

Figure B.9. DGS for a 0.50 cm flaw located at $x=-.625$, $z=1.25$ cm in a 2.5 cm aluminum cylinder. $P_{50} = 1$, $T = 61079$ sec.

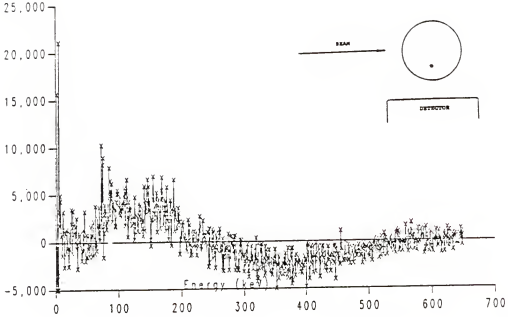

Figure B.10. DGS for a 0.50 cm flaw located at x=0.625, z=0.625 cm in a 2.5 cm aluminum cylinder. P_{50} = 1, T = 61079 sec.

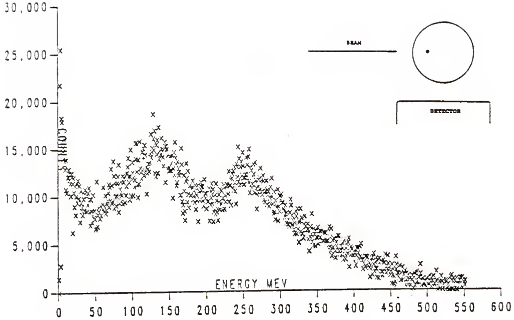

Figure B.11. DGS for a 0.25 cm flaw located at x=0, z= 0.625 cm in a 2.5 cm aluminum cylinder.

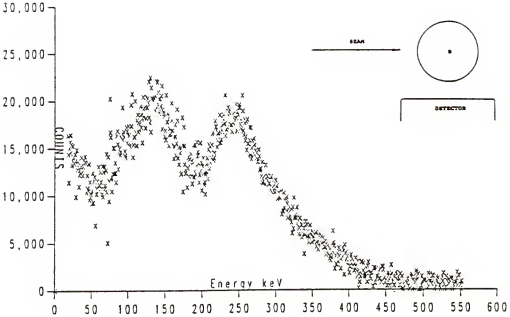

Figure B.12. DGS for a 0.25 cm flaw located at x=0, z= 1.25 cm in a 2.5 cm aluminum cylinder. P_{50} =1, T = 68878 sec.

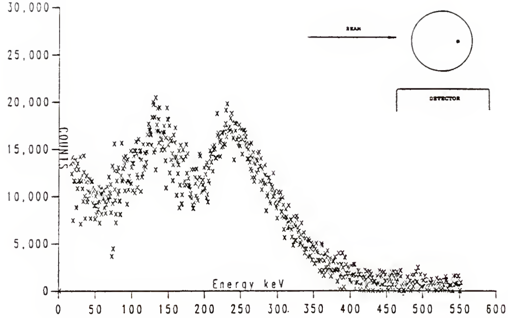

Figure B.13. DGS for a 0.25 cm flaw located at x=0, z= 1.875 cm in a 2.5 cm aluminum cylinder. P_{50} = 1, T = 68878 sec.

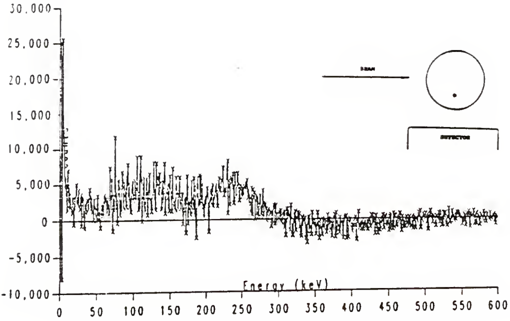

Figure B.14. DGS for a 0.25 cm flaw located at x=0.625,k z= 1.25 cm in a 2.5 cm aluminum cylinder. P_{50} = 0, T = 68878 sec.

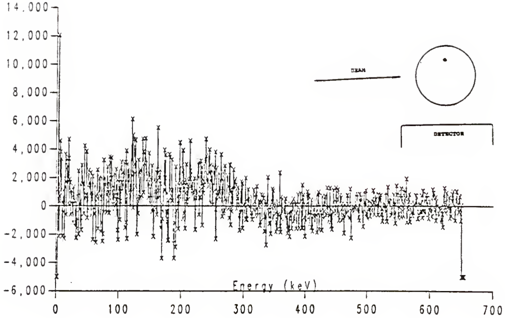

Figure B.15. DGS for a 0.25 cm flaw located at $x=-.625$, $z=1.25$ cm in a 2.5 cm aluminum cylinder. $P_{50} = 0$, $P_{30} = .493$, $T = 69725$ sec.

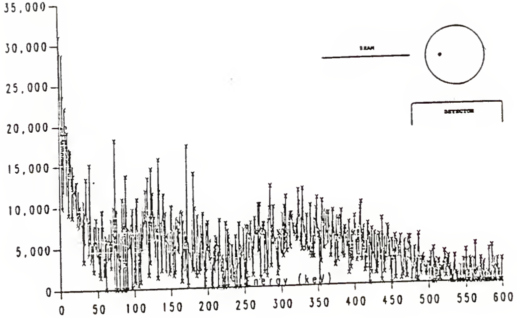

Figure B.16. DGS for a 0.10 cm flaw located at x=0, z= 0.625 cm in a 2.5 cm aluminum cylinder. P_{50} = .898, T = 124402 sec.

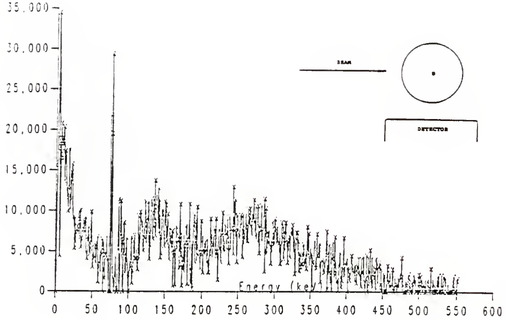

Figure B.17. DGS for a 0.10 cm flaw located at x=0, z=1.25 cm in a 2.5 cm aluminum cylinder. P_{50} = .893, T = 124402 sec.

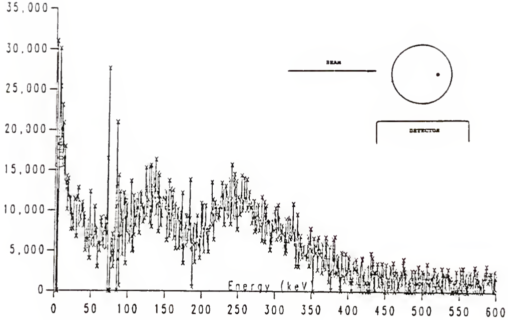

Figure B.18. DGS for a 0.10 cm flaw located at x=0, z=1.875 cm in a 2.5 cm aluminum cylinder. P_{50} = 1, T = 124402 sec.

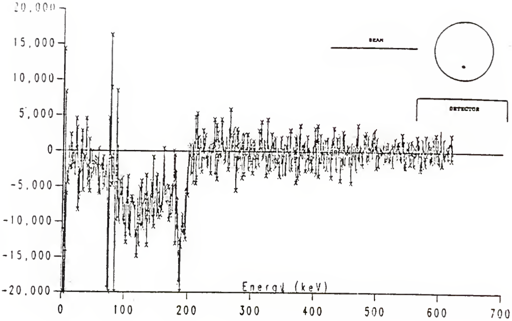

Figure B.19. DGS for a 0.10 cm flaw located at $x=.625$, $z= 1.25$ cm in a 2.5 cm aluminum cylinder. $P_{50} = 0$, $T = 128119$ sec.

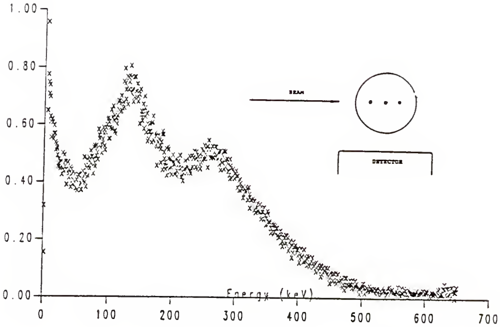

Figure B.20. DGS for three flaws located along the illuminated chord.

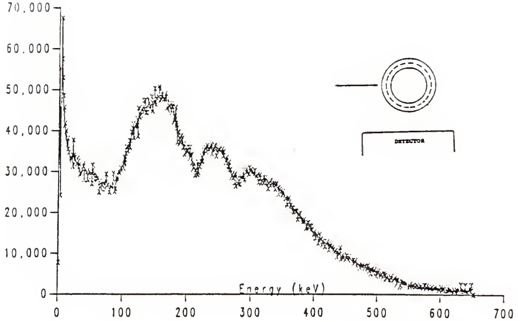

Figure B.21. DGS for a 0.635 cm thick, 3.81 cm pipe with 0.3175 cm thinning on outside wall. P_{50} = 1.

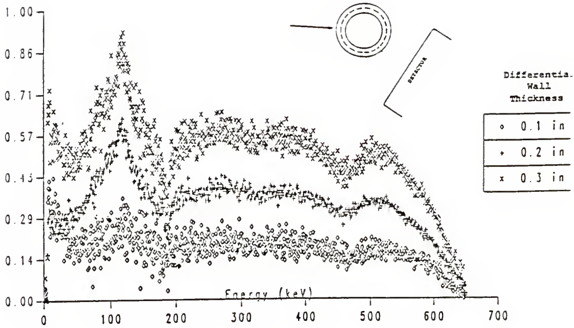

Figure B.22. DGS from a 5.08 cm O.D. pipe with a nominal 2.54 cm inner diameter showing internal wall thinning.

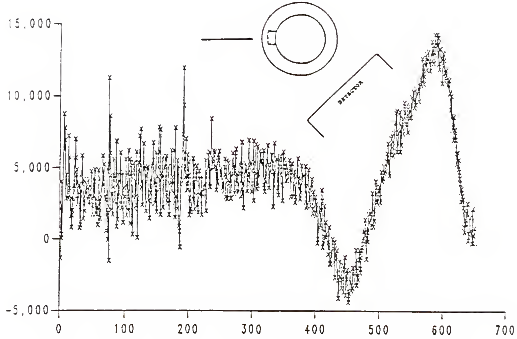

Figure B.23. DGS for a 0.635 cm diameter pit in a .3175 cm thick, 3.81 cm diameter pipe located at x=0 and z=3.175 cm. Detector: x = 3.05 cm, z = 5.97 cm, angle = 37°. P_{50} = 1.

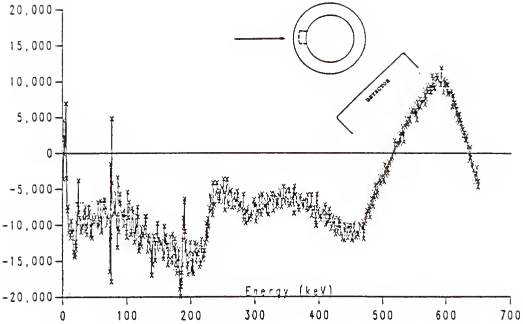

Figure B.24. DGS for a 1.27 cm diameter pit in a .318 cm thick, 3.81 cm diameter pipe located at x = 0 and z= 3.18 cm. Detector: x = 3.05 cm, z = 5.97 cm, angle = 37°. P_{50} = 1.

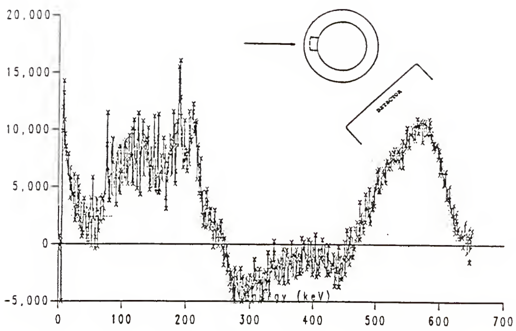

Figure B.25. DGS for a 0.635 cm wide gouge in a .318 cm thick, 3.81 cm diameter pipe located at x=0 and z = 3.18 cm. Detector: x = 3.05 cm, z = 5.97 cm, angle = 37°. $P_{50} = 1$.

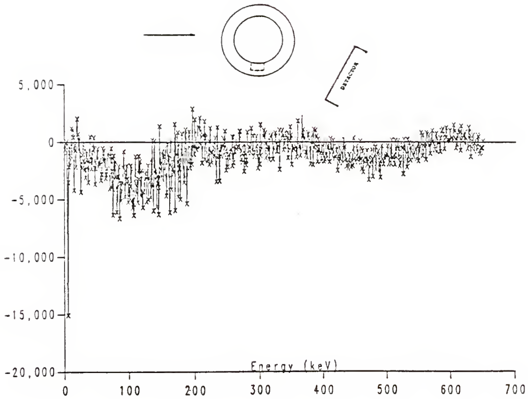

Figure B.26. DGS for a 1.27 cm diameter pit in a .318 cm thick, 3.81 cm diameter pipe located at x=1.27 cm and z=1.91 cm. Detector: x = 3.05 cm, z = 5.97 cm, angle = 37°. P_{50} = 0.0.

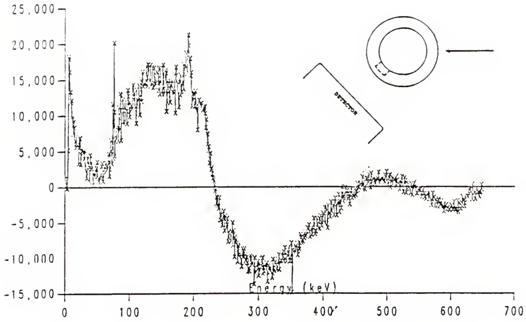

Figure B.27. DGS for a .635 cm diameter pit in a .318 cm thick, 3.81 cm diameter pipe located at x=.635 cm, z= 3.175 cm. Detector: x = 3.048 cm, z = 5.97 cm, angle = 37^0. P_{50} = 1.

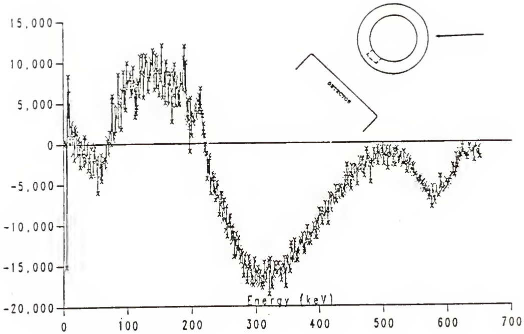

Figure B.28. DGS for a .635 cm diameter pit in a .318 cm thick, 3.81 cm diameter pipe located at x = .1762 cm and z = 2.92 cm. Detector: x = 3.05 cm, z = 5.97 cm, angle = 37°. P_{50} = 1.

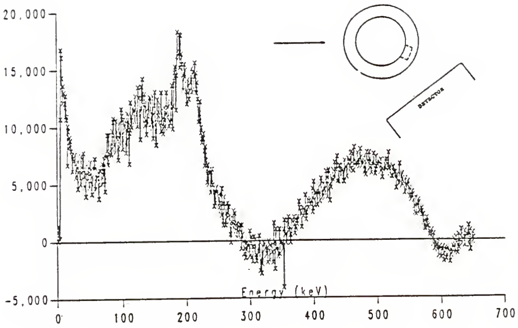

Figure B.29. DGS for a 1.27 cm diameter pit in a .318 cm thick, 3.81 cm diameter pipe located at x = 0 and z = 3.18 cm. Detector: x = 3.05 cm, z = 5.97 cm, angle = 37°. P_{50} = 1.

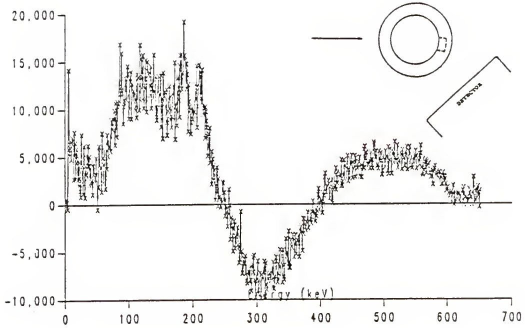

Figure B.30. DGS for a .635 cm diameter gouge in a 0.318 cm thick, 3.81 cm diameter pipe located at x = 0 and z = 3.18 cm. Detector: x = 3.05 cm, z = 5.97 cm, angle = 37°. P_{50} = 1.

REFERENCES

1. Odeblad, E., Norhagen, A., "Electron Density in a Localized Volume by Compton Scattering," Acta Radiologica, 45, 161 (1959).

2. Kaufman, L., G. Gamsu, C. Savoca, and S. Swarm, "X- and Gamma-Ray Sources and Applications," CONF-760539, Proc. ERDA Symposium on X- and Gamma-Ray Sources and Applications, 151-154, Ann Arbor, Michigan (May 19-21, 1976).

3. Costello, D.G., J.A. Stokes, and A.P. Trippe, "Theory and Applications of Collimated Photon Scattering," 14th Symposium on Nondestructive Evaluation, San Antonio Texas (April 19-21, 1983).

4. Anghaie, S., "Accuracy Improvement for Gamma-Ray Techniques in Two Phase Methods," Ph.D. Dissertation, Pennsylvania State University, Nuclear Engineering (1982).

5. Tagart, S.W., Jr., "Effects of NDE on Piping Reliability," Special Report, Electric Power Research Institute NP-4315-SR, Nondestructive Evaluation Program: Progress in 1985, section 5, Palo Alto (May 1986).

6. Kraufkramer, J, H. Kraufkramer, Ultrasonic Testing of Materials, Springer-Verlag, Berlin (1983).

7. Wustenberg, H., A. Erhard, "Development of Ultrasonic Techniques for Sizing Defects," Non-destructive Examination in Relation to Structural Integrity, Applied Science Publishing, London (1980).

8. Alippi, A., W.G. Mayer (Editors), Ultrasonic Methods in Evaluation of Inhomogeneous Materials, Martinus Nijhoh Publishers, Dordrecht (1987).

9. Klein, O., Nishina, Y., "Scattering of Radiation by Free Electrons on the New Relativistic Quantum Dynamics of Dirac", Zeits. f. Physik, 52, 853 (1929).

10. Mix, Paul. E., P.E., Introduction to Nondestructive Testing: A Training Guide, John Wiley & Sons, New York (1983).

11. Cho, Z.H., I. Ahn, C. Bohn, and G. Hull, "Computerized Image Reconstruction Methods with Multiple Photon/x-ray Transmission Scanning," Phys. Med. Biol, 19, No.4, 511-522 (1974).

12. Gordon, R., G. Herman, S. Johnson, "Image Reconstruction from Projections," Scientific American, 39, 56-68 (October 1975).

13. Kondic, N.N., A.M. Jacobs, S. Anghaie, "Non-Intrusive Determination of Mass Density Distribution by Gamma-Ray Scattering Historical Survey and Perspectives," American Society of Mechanical Engineers / Fluids Engineers Conference, Cavitation and Multiphase Flow Forum, Albuquerque, (June 1985).

14. Anghaie, S., A.M. Jacobs, N.N. Kondic, "Application of Gamma Scattering Compton Profile for Two-Phase Systems Densitometry," invited paper, American Nuclear Society Winter Meeting, San Francisco, (November 1981).

15. Bodette, D. "Tomographic Two-Phase Flow Measurement Using Compton Scattering of Gamma-Rays," Ph.D. Dissertation, University of Florida, Nuclear Engineering (1986).

16. Bobo, S.N., "A Handbook for Infrared Non-Destructive Boiler Tube Inspection," Final Report, Nondestructive Inspection Systems for Boiler Tubes, Electric Power Research Institute CS-4742, Palo Alto (August 1986).

17. Wheeler, Jane. B. (Editor), Eddy Current Characterization of Materials and Structures, American Society for Testing and Materials, Philadelphia (September 1979).

18. Diaz, N.J., S. Anghaie, Flaw Detection, Sizing and Location by Differential Gamma Scattering Spectrum Technique, Final Report, NSF-MEA-8460940 (August 1985).

19. Anghaie, S., N.J. Diaz, "Differential Gamma Scattering Spectrum Characterization of Materials and Flaws," Proc. ASNT 1988 Sprint Conference on Characterization of Materials and Flaws, Orlando (April 1988).

20. Anghaie, S., N.J. Diaz, "High Resolution NDE with Differential Gamma Scattering Spectrum Technique," Advances in Test Measurements, 23, 384-408 (May 1986).

21. Jacobs, A.M., "Compton Profile Radiography," International Advances in Nondestructive Testing, 12, 17-52, Gordon and Branch, New York (1986).

22. Knoll, G.F., Radiation Detection and Measurement, John Wiley & Sons, New York (1979).

23. Fano, V., L. Spencer, M. Berger, Encyclopedia of Physics, S. Flugge (Ed.), Springer-Verlag, New York (1959).

24. Wood, J., Computational Methods in Reactor Shielding, Pergammon Press, Oxford (1982).

25. Duderstadt, J., Martin, W., Transport Theory, John Wiley & Sons, New York (1979).

26. Routti, J.T. J.V. Sandburg, "Unfolding Techniques for Activation Detector Analysis," Computer Techniques in Radiation Transport and Dosimetry, Plenum Press, New York (1980).

27. Ribberfors, "Relationship of the Relativistic Compton Cross-section to the momentum distribution of Bound Electrons," Phys. Rev., B12, 2067, (1975).

28. Cooper, M., P. Pattison, J.D. Schneider, "Compton Profile Measurements with 412 keV gamma-rays," Phil. Mag., 34, 243 (1976).

29. Halonen, V., B.G. Williams, T. Paakkari, "Multiple Scattering in the Compton Effect III Monte Carlo Calculation," Phys. Rev., A., 14, 328 (1976).

30. Williams, Brian (Editor), Compton Scattering, McGraw-Hill, London (1977).

31. Friedlander, G., J.W. Kennedy, E.S. Macias, J.M. Miller, Nuclear and Radiochemistry, John Wiley and Sons, New York (1981).

32. Rust, B.W., W.R. Burros, Mathematical Programming and the Numerical Solution of Linear Equations, American Elsevier, New York (1972).

33. Richman, R.H., T.W. Rettig, S.R. Paterson, Nondestructive Inspection Systems for Boiler Tubes, Final Report, Electric Power Research Institute, CS-4742, Palo Alto (August 1986).

34 Schaeffer, N.M., Reactor Shielding for Nuclear Engineers, U.S. Atomic Energy Commission TID-25951 (1973).

BIOGRAPHICAL SKETCH

Larry Humphries was born on May 10, 1960, in Twin Falls, Idaho. He graduated from Buhl High School in Buhl, Idaho, in June of 1978. In May of 1983, he received a Bachelor of Science degree in general engineering (with a nuclear option) from Idaho State University. He graduated with honors.

In May of 1987, Larry Humphries received his Master of Science degree in nuclear engineering with a minor in mathematics from Oregon State University. The topic of his thesis research was an assessment of the hazards and risks of transporting radioactive materials through the state of Oregon. As part of his research he helped train more than a thousand emergency response personnel throughout the Northwest to respond to traffic accidents involving radioactive materials. He also prepared a protective action guide for the state of Oregon to be used by emergency responders at an accident site. Larry has written over ten articles on radioactive materials transportation that have appeared in technical journals or at professional conferences.

In 1986 Larry Humphries came to Florida to continue studies in nuclear engineering and material sciences at the University of Florida. He expects to receive a Doctor of Philosophy from the University of Florida in May 1989.

I certify that I have read this study and that in my opinion it conforms to acceptable standards of scholarly presentation and is fully adequate, in scope and quality, as a dissertation for the degree of Doctor of Philosophy.

Samim Anghaie

Samim Anghaie, Chairman
Associate Professor of Nuclear
Engineering Sciences

I certify that I have read this study and that in my opinion it conforms to acceptable standards of scholarly presentation and is fully adequate, in scope and quality, as a dissertation for the degree of Doctor of Philosophy.

Nils J. Diaz
Professor of Nuclear Engineering
Sciences

I certify that I have read this study and that in my opinion it conforms to acceptable standards of scholarly presentation and is fully adequate, in scope and quality, as a dissertation for the degree of Doctor of Philosophy.

Edward T Dugan

Edward T. Dugan
Associate Professor of Nuclear
Engineering Sciences

I certify that I have read this study and that in my opinion it conforms to acceptable standards of scholarly presentation and is fully adequate, in scope and quality, as a dissertation for the degree of Doctor of Philosophy.

Alan M. Jacobs

Alan M. Jacobs
Professor of Nuclear Engineering
Sciences

I certify that I have read this study and that in my opinion it conforms to acceptable standards of scholarly presentation and is fully adequate, in scope and quality, as a dissertation for the degree of Doctor of Philosophy.

Robert J Hanrahan

Robert J. Hanrahan
Professor of Chemistry

I certify that I have read this study and that in my opinion it conforms to acceptable standards of scholarly presentation and is fully adequate, in scope and quality, as a dissertation for the degree of Doctor of Philosophy.

Robert E. Reed-Hill

Robert E. Reed-Hill
Professor of Materials Science and Engineering

This dissertation was submitted to the Graduate Faculty of the College Engineering and to the Graduate School and was accepted as partial fulfillment of the requirements for the degree of Doctor of Philosophy.

May 1989

Hubert A. Bevis

Dean, College of Engineering

Dean, Graduate School